Thermoelastic analysis of sandwich conical shells with GPLs reinforced face sheets and porous core under moving thermomechanical loading

Parviz Malekzadeh [1], Yasin Heydarpour[1*], Hanxing Zhu[2*]

[1] *Department of Mechanical Engineering, School of Engineering, Persian Gulf University, Bushehr 7516913798, Iran*

[2] *School of Engineering, Cardiff University, Cardiff CF24 3AA, UK*

The thermoelastic responses of the sandwich truncated conical shells with graphene platelets (GPLs) reinforced composite face sheets and GPLs reinforced composite porous core subjected to ring-shape moving thermo-mechanical loading are studied. In order to capture the influences of the finite heat wave speed and the thermo-mechanical coupling, the Lord-Shulman thermoelasticity theory, which has no kinematical assumption such as those used in the two-dimensional theories, is employed to accurately estimate the thermoelastic behaviors of the sandwich shells. A layerwise hybrid numerical technique composed of the differential quadrature method and multi-step based NURBS method is applied to discretize the strong form of the equations in the spatial and temporal domains, respectively. Also, the boundary and compatibility conditions at the interfaces of the layer are exactly implemented at the corresponding grid points. After validating the proposed approach, parametric studies are conducted and discussed to explore the impacts of the porosity amount and distribution, GPLs weight fractions, thermo-mechanical load velocity, edge boundary conditions and some other parameters on the thermoelastic behaviors of the sandwich shells. The results indicate that the increase of the GPLs weight fraction decreases the displacement and changes its distribution along the shell thickness but does not affect the stress distribution. Also, the porosity distribution pattern changes the displacement distribution, and the displacement has the lowest values when the porosity is higher near the inner surface of the core layer.

* Corresponding author. Tel.: +98 77 31222150; fax: +98 77 33440376
E-mail addresses: heydarpour@pgu.ac.ir (Yasin Heydarpour).

* Corresponding author. Tel.: +44 (0) 29 2087 4824
E-mail addresses: zhuh3@cardiff.ac.uk (Hanxing Zhu).

Keywords: Sandwich conical shells; Nanocomposite face sheets; Porous core; Lord-Shulman theory; Moving thermo-mechanical loading; GPLs.

1. Introduction

Due to their high structural performances and also design requirements, truncated conical shells have found a wide range of applications in different fields of engineering such as marine, aerospace, civil and mechanical engineering; for example, in underwater vehicles, aircraft propulsion systems, spacecraft, missiles and reactors [1-6]. To achieve high-performance lightweight conical shells, composite materials have been used to form these types of structural elements. Among them, sandwich materials are commonly used to build up shells of different shapes [7, 8]. The sandwich materials are composed of a relatively thick soft and low-density layer placed between two thin but stiff layers. The core layer is usually made of cellular polymeric foam materials, metallic and non-metallic honeycombs, balsa wood or trusses. Also, the face sheets are structured from laminated composite materials or metals such as aluminum.

Nowadays, the advances in manufacturing technologies, particularly conception of 3D printing [9-13], have permitted the scientists in the related field to create high-performance new composite materials by replacing the micro-sized reinforcements with the nano-sized fillers, which can be used as the face sheets of sandwich materials for advanced technologies. One of the important and emerging nanofillers is graphene platelets (GPLs) [14-16]. These very thin flat monolayer nanomaterials are structured by joining carbon atoms in a hexagonal lattice pattern. GPLs have ease and low cost of manufacturing in comparison to graphene and its other derivatives, in addition to extraordinary properties such as Young's modulus, strength, thermal conductivity, electrical conductivity and chemical stability [17-19]. It has been explored that addition of small amount of GPLs in any matrix materials results in a significant improvement of the mechanical properties of the resulting advanced nanocomposites [19].

Despite some advantages of porosities in the core layer of sandwich shells such as low density, sound isolation, impact and thermal resistance, they reduce the overall stiffness of the resulted composite shells. However, the porosities in the core layer can be tailored to satisfy the required performance [20,21]. On the other hand, it has been shown that reinforcing the porous materials with a small amount of GPLs can compensate this effect and enhance their stiffness [22,23]. Thus,

without increasing its thickness or its weight considerably, the porous core layer can also be reinforced by GPLs to recover its lost stiffness.

The mechanical and thermo-mechanical behaviors of the truncated conical shells made of different homogeneous and composite materials have been investigated in recent years [24-29]. In continuation, some of these works are briefly reviewed.

Yang et al. [30] employed the first-order shear deformation theory (FSDT) under the von-Kármán nonlinear geometric assumptions to investigate the nonlinear free vibration behaviors of a functionally graded graphene platelet-reinforced composite (FG-GPLRC) truncated conical shell. They applied the Galerkin method together with the harmonic balance method (HBM) to analytically estimate the nonlinear frequencies of the shell. Baranifard et. al. [31] studied the free vibration characteristics of the point supported sandwich truncated conical shells with GPLRC face sheets and porous core using a first-order shear deformation-based zigzag shell theory. They utilized linear elastic springs to simulate the point supports and solve the problem by applying the Ritz method with Chebyshev polynomials multiplied by some boundary functions as its admissible basis functions (the so-called Chebyshev-Ritz method). Youseftabar et al. [32] introduced an analytical approach to present the nonlinear free vibrational behavior of a porous cone-shaped shell surrounded by an elastic media based on the FSDT subjected to von Kármán large deformation assumptions. They determined the nonlinear frequencies by means of the Galerkin decomposition and the harmonic balance methods. By using the traveling wave vibration analysis, Li et al. [33] studied the nonlinear vibration characteristics of rotating sandwich conical shell with GPLRC porous core and aluminum face sheets. They modeled the shell deformation according to the FSDT and von Kármán nonlinear geometric nonlinear assumptions. The nonlinear vibration behaviors of axially moving porous GPLRC truncated conical shells were discussed in a research work by Huang et al. [34]. They derived the shell motion equations in the context of the classical shell theory and utilized the Galerkin method to extract frequencies. Khoddami Maraghi et al. [35] explored the effects of GPLs distribution patterns and the shell geometric parameters on the linear free vibration frequencies of a sandwich truncated conical shell with a re-entrant auxetic core and GPLRC face sheets based on the FSDT of shells. A combination of the trigonometric functions and the differential quadrature method (DQM) was employed to spatially discretize the motion equations and the related boundary conditions.

Huang et al. [36] reported the static stability of porous FG-GPLRC truncated conical shells loaded by hydrostatic pressure and axial tension. They obtained the critical buckling hydrostatic pressure and axial tension using the Galerkin method. Bahranifard et al. [37,38] studied the linear and nonlinear dynamic responses of the ring-stiffened sandwich truncated conical shells with GPLRC face sheets and porous core under a moving ring-shaped pressure loading based on the FSDT of shells. They obtained the linear solution by employing the Ritz method with Chebyshev polynomials multiplied by some boundary functions as its admissible basis functions (the so-called Chebyshev-Ritz method) and Newmark time integration technique. The large amplitude responses were extracted using the same approach but by considering the von Kármán geometric nonlinearity assumptions and additionally applying the Newton-Raphson method. Gao et al. [39] investigated the random vibration of FG-GPLRC conical shells due to base acceleration excitation by applying a combination of the spectro-geometric method and the pseudo-excitation method in the framework of the FSDT. Li et al. [40] analyzed the stochastic vibration responses of FG-GPLRC truncated conical shells subjected to meridional and circumferential moving random loads.

Heydarpour et al. [41] estimated the thermoelastic responses of rotating FG-GPLRC truncated conical shells under a standing thermal shock loading based on the Lord-Shulman thermoelasticity theory. They employed the transformed differential quadrature method (TDQM) and a multi-step time integration scheme based on a non-uniform rational B-spline (NURBS) interpolation to solve the governing differential equations. Mohammadlou et al. [42] carried out the analysis on the steady state axisymmetric thermoelastic responses of a homogeneous thin-walled conical shell subjected to uniform heat flow along its side surfaces. They assumed the thermal insulation at both ends of shell and utilized the Galerkin finite element method to solve the semi-coupled steady state thermoelastic equations. Recently, Heydarpour et al. [43] analyzed the thermal behavior of the sandwich truncated conical shells with GPLRC face sheets and GPLRC porous core under a moving heat flux using a non-Fourier heat conduction law. The thermoelastic deformation of the shell under thermo-mechanical loading was not studied in this work.

To the best of our knowledge, the thermoelastic analysis of the sandwich truncated conical shells with GPLRC face sheets (GPLRC-FSs) and GPLRC porous core (GPLRC-PC) subjected to moving thermo-mechanical load has not been investigated yet. Due to their wide range of applications of composite truncated conical shells in aerospace engineering and other advanced industries, these types of thermoelastic problems have both academic value and industrial

applications. On the other hand, the accurate predication of the thermoelastic behaviors of the sandwich truncated conical shells manufactured with GPLRC-FSs and GPLRC-PC under moving thermo-mechanical loading has a key role in their design and construction, typically adopted as structural components in aircrafts, or as loudspeaker cones in the music industry. In addition, it is an important and challenging problem from the academic point of view and it essential to develop a computationally efficient and simple numerical approach based on a relatively complete and accurate theory. Therefore, this work aims to provide an insight into the thermoelastic responses of these types of sandwich truncated conical shells under ring-shape moving thermo-mechanical loading. In order to capture the effect of thermos-mechanical shock loading, the Lord-Shulman thermoelasticity theory is chosen. On the other hand, an efficient and accurate numerical method is necessary for in-depth study of this complicated problem. To carry out this task, the Lord-Shulman is employed to develop the thermoelastic equations of each layer of the sandwich shells in a layerwise manner. In addition, the natural compatibility conditions at the interface of the two adjoining layers together with the external boundary conditions at the inner surface, outer surface and the ends of the shell are explained and imposed exactly on the related surfaces. One advantage of this method over the other methods that used the weak form of the equations is that the strong form of the equations and the related boundary and natural compatibility conditions at the corresponding points are discretized. The verification and reliability of the present approach are completed by showing its convergence behavior and doing comparison studies with some available solutions in the limit cases. After that, the influences of the load velocity, porosity distribution and amounts, GPLs weight fractions and the shell geometric parameters on the thermoelastic responses of the sandwich truncated conical shells with GPLRC-FSs and GPLRC-PC are presented and discussed.

2. Mathematical modelling

The sandwich conical shells to be studied are composed of two GPLRC face sheets and a GPLRC core layer (Fig. 1) and have a length L, the smallest inner radius R_1, the largest inner radius R_2, semi-vertex angle β, mean radius R_m (at its middle section) and total thickness h (see Fig. 1a). The core layer and the face sheets are manufactured from a GPLs reinforced porous material and a GPLs reinforced polymer matrix, respectively, and it is assumed that the layers are perfectly bonded. In both core layer and face sheets, GPLs are uniformly distributed and randomly oriented.

In this work, the shells are under an axisymmetric ring-shape moving thermo-mechanical loading, which enter the shell with a constant velocity at the section z=0 and leave it at the section $z= L\cos\beta$. On the other hand, the shells have axisymmetric geometry, material properties, and boundary conditions. Thus, a cylindrical coordinate system with coordinate variables (r,z) is appropriate and sufficient to detect the material points of the shells in the unreformed reference state (Fig. 1 (a)). In continuation, the relations and equations that govern the transient thermoelastic responses of the sandwich shells with GPLRC-FSs and GPLRC-PC subjected to moving thermos-mechanical moving are reported.

2.1 Material properties and the constitutive relations of GPLRC-FSs and GPLRC-PC

To estimate the effective material properties of the GPLRC materials, it is assumed that the in-plane properties of the individual GPLs are isotropic [19]. On the other hand, by considering that the rectangular GPLs are uniformly distributed and randomly oriented in the isotropic polymer matrix, the resulted nanocomposite becomes an isotropic and homogeneous material. Thus, its equivalent Young's modulus can be obtained in terms of the GPL dimensions and volume fraction (V_{GPL}), and the matrix Young's modulus (E_m) using the modified Halpin-Tsai micromechanical model, and described by [9]

$$E=\left(\frac{3}{8}\frac{1+\zeta_L\eta_L V_{GPL}}{1-\eta_L V_{GPL}}+\frac{5}{8}\frac{1+\zeta_T\eta_T V_{GPL}}{1-\eta_T V_{GPL}}\right)E_m \tag{1}$$

The dimensionless parameters ζ_i and η_i (i=L,T) are related to the dimensions, the Young's modulus of GPLs, and the Young's modulus of matrix, and given as [19]

$$\zeta_L=2\left(a_{GPL}/t_{GPL}\right)=2\left(a_{GPL}/b_{GPL}\right)\left(b_{GPL}/t_{GPL}\right),\zeta_T=2\left(b_{GPL}/t_{GPL}\right),\eta_L=\frac{\left(E_{GPL}/E_m\right)-1}{\left(E_{GPL}/E_m\right)+\zeta_L},$$

$$\eta_T=\frac{\left(E_{GPL}/E_m\right)-1}{\left(E_{GPL}/E_m\right)+\zeta_T} \tag{2a-d}$$

where a_{GPL}, b_{GPL}, t_{GPL} and E_{GPL} denote the length, width, thickness and Young's modulus of GPLs, respectively.

The remainder properties of GPLRC material are determined using the simple mixture rule [19,44,45]

$$\rho = \rho_m V_m + \rho_{GPL} V_{GPL} \tag{3}$$

$$\nu = \nu_m V_m + \nu_{GPL} V_{GPL} \tag{4}$$

$$c = c_m V_m + c_{GPL} V_{GPL} \tag{5}$$

$$\alpha = \alpha_m V_m + \alpha_{GPL} V_{GPL} \tag{6}$$

where ρ, ν, c and α are the mass density, Poisson's ratio, specific heat capacity and thermal expansion coefficient of GPLRC, respectively. Also, the parameters with the subscripts "*m*" and "*GPL*" represent the counterpart parameters of the matrix and GPLs, respectively. The relation between the GPLs and matrix volume fractions is $V_m + V_{GPL} = 1$.

It is clear that the measurement of the GPLs weight fraction is easier than their volume fraction. Thus, it is preferred to express the GPLs volume fraction by the related weight fraction $\left(w_{GPL}\right)$ and consider it as input data when reporting the extracted numerical results

$$V_{GPL} = \frac{w_{GPL}}{w_{GPL} + \left(\rho_{GPL}/\rho_m\right)\left(1 - w_{GPL}\right)} \tag{7}$$

The effective thermal conductivity of the GPLRC material (k) is estimated by the formulation suggested by Chu et al. [28,29]

$$\frac{k}{k_m} = \frac{2/3\left(V_{GPL} - 1/p\right)^{\gamma}}{H(p) + 1/\left(k_{GPL}/k_m - 1\right)} + 1 \tag{8}$$

where $p = a_{GPL}/t_{GPL}$, γ is a fitting parameter and $H(p)$ is a dimensionless geometric function [46,47]

$$H(p) = \frac{\ln\left(p + \sqrt{p^2 - 1}\right)p}{\sqrt{\left(p^2 - 1\right)^3}} - \frac{1}{p^2 - 1} \tag{9}$$

It is clear that the porosities influence the thermo-mechanical properties of the materials. To engineer the porosity distribution to achieve the required material properties, it is usually preferred to distribute the porosities along the thickness direction in a functionally graded (FG) manner. In the present work, three FG porosity distribution patterns that have been used by other researchers are considered. The effective Young's modulus (E), density (ρ), specific heat capacity (c) and thermal conductivity (k) of the porous core are estimated, respectively, according to the following equations [37,38],

$$E(r)=E_c\left[1-\Xi(r,e_0)\right],\ \rho(r)=\rho_c\left[1-\Xi(r,e_m)\right],c(r)=c_c\left[1-\Xi(r,e_0)\right],\ k(r)=k_c\left[1-\Xi(r,e_0)\right] \quad (10a\text{-}d)$$

where E_c, ρ_c, c_c and k_c are the effective Young's modulus, density, specific heat capacity and thermal conductivity of the perfect GPLR core, respectively. In addition, the porosity functions $\Xi(z,e_0)$ of the considered different distribution patterns are as follows [37,38]

Type 1: $\Xi(z,e_\chi)=e_\chi\cos[\pi(0.5-\bar{r})]$

Type 2: $\Xi(z,e_\chi)=1-e_\chi\cos[\pi(0.5-\bar{r})]$

Type 3: $\Xi(z,e_\chi)=e_\chi\cos(0.5\bar{r}\pi)$ (11a-c)

where $\bar{r}=\left[\dfrac{r-R_i(z)}{h\sec\beta}\right]$, which indicates that $0\le\bar{r}\le1$, and $\chi=0,m$. Also, the porosity coefficients $e_\chi(\chi=0,m)$ are determined as [37,38]

$$e_0=1-\frac{\rho_{\min}}{\rho_c},\ e_m=1-\sqrt{1-e_0} \quad (12a,b)$$

where $\rho_{\min}$ is the minimum density of the GPLR porous core. In this work, to provide a rational comparison studies when using different porosity distribution patterns, the GPLR porous cores with the same mass are examined.

The stress tensor components $\sigma_{ij}\ (i,j=r,\theta,z)$ of the shell layer are related to the strain tensor components $\varepsilon_{ij}\ (i,j=r,\theta,z)$ through the following constitutive relations [41]

$$\begin{Bmatrix}\sigma_{rr}\\ \sigma_{\theta\theta}\\ \sigma_{zz}\\ \sigma_{rz}\end{Bmatrix}=\begin{bmatrix}C_{11}&C_{12}&C_{13}&0\\ C_{12}&C_{22}&C_{23}&0\\ C_{13}&C_{23}&C_{33}&0\\ 0&0&0&C_{55}\end{bmatrix}\begin{Bmatrix}\varepsilon_{rr}\\ \varepsilon_{\theta\theta}\\ \varepsilon_{zz}\\ 2\varepsilon_{0rz}\end{Bmatrix} \quad (13)$$

where the strain tensor components $\varepsilon_{ij}\ (i,j=r,\theta,z)$ are related to the displacement components by

$$\varepsilon_{rr}=\frac{\partial u}{\partial r},\ \varepsilon_{\theta\theta}=\frac{u}{r},\ \varepsilon_{zz}=\frac{\partial w}{\partial z},\ 2\varepsilon_{rz}=\frac{\partial u}{\partial z}+\frac{\partial w}{\partial r} \quad (14a\text{-}d)$$

where u and w are the displacement components along the radial and axial directions at a material point of the shell. Also, the material stiffnesses C_{ij} are related to the material elastic constants as follows [41]

$$C_{11}=C_{22}=C_{33}=\frac{(1-\nu)E}{(1+\nu)(1-2\nu)},C_{12}=C_{23}=C_{13}=\frac{\nu E}{(1+\nu)(1-2\nu)},C_{55}=\frac{E}{2(1+\nu)} \quad (15a\text{-}c)$$

2.2. Transient thermoelastic analysis

In this subsection, the differential equations governing the transient thermoelastic responses of the sandwich truncated conical shells with the GPLRC-FS and GPLRC-PC under internal axisymmetric moving heat flux and pressure loading are presented. These equations include the thermo-mechanical energy balance equation and the thermoelastic equations of motion together with the corresponding constitutive relations. Due to axisymmetric geometry, material, boundary conditions and mechanical loading conditions, the field variables do not vary along the tangential direction. Considering this point, the governing equations together with the related external boundary and compatibility conditions at the interface of two adjacent layers of the shell will be obtained in terms of the displacement components and temperature.

The thermo-mechanical energy balance equation for each nanocomposite layer of the sandwich shell based on the Lord–Shulman thermoelasticity theory can be expressed as [48]

$$\frac{1}{r}\frac{\partial}{\partial r}\left(rk\frac{\partial T}{\partial r}\right)+\frac{\partial}{\partial z}\left(k\frac{\partial T}{\partial z}\right)=\rho c\left(\frac{\partial T}{\partial t}+\tau_0\frac{\partial^2 T}{\partial t^2}\right)+\alpha(3\lambda+2\mu)T_0\left(\tau_0\frac{\partial^2}{\partial t^2}+\frac{\partial}{\partial t}\right)\left(\frac{\partial u}{\partial r}+\frac{u}{r}+\frac{\partial w}{\partial z}\right) \quad (16)$$

where T is the temperature at a material point of the shell, T_0 the stress-free temperature of the shell, t the time and τ_0 the relaxation time of the Lord–Shulman thermoelasticity theory. Also, the Lamé's elastic constants (i.e., λ and μ) are related to the shell Young's modulus and Poisson's ratio as $\lambda=\frac{E\nu}{(1+\nu)(1-2\nu)}$ and $\mu=\frac{E}{2(1+\nu)}$.

The equations of motion along the radial and axial directions are summarized as follows, respectively

δu :

$$rC_{11}\frac{\partial^2 u}{\partial r^2}+\left(r\frac{dC_{11}}{dr}+C_{12}\right)\frac{\partial u}{\partial r}+rC_{55}\frac{\partial^2 u}{\partial z^2}+\left(\frac{dC_{12}}{dr}-\frac{C_{22}}{r}\right)u+\left(r\frac{dC_{13}}{dr}+C_{13}-C_{23}\right)\frac{\partial w}{\partial z}+$$
$$r\left(C_{55}+C_{13}\right)\frac{\partial^2 w}{\partial r\partial z}=r\rho\frac{\partial^2 u}{\partial t^2}+r\left(\frac{dC_{11}}{dr}+\frac{dC_{12}}{dr}+\frac{dC_{13}}{dr}\right)\alpha\Delta T$$
$$+r\left(C_{11}+C_{12}+C_{13}\right)\frac{\partial}{\partial r}\left(\alpha\Delta T\right) \tag{17}$$

δw :

$$\left(r\frac{dC_{55}}{dr}+C_{23}+C_{55}\right)\frac{\partial u}{\partial z}+r\left(C_{13}+C_{55}\right)\frac{\partial^2 u}{\partial r\partial z}+rC_{55}\frac{\partial^2 w}{\partial r^2}+\left(r\frac{dC_{55}}{dr}+C_{55}\right)\frac{\partial w}{\partial r}+rC_{33}\frac{\partial^2 w}{\partial z^2}$$
$$=r\left(C_{13}+C_{23}+C_{33}\right)\frac{\partial}{\partial z}\left(\alpha\Delta T\right)+r\rho\frac{\partial^2 w}{\partial t^2} \tag{18}$$

where $\Delta T=T-T_0$.

The inner surface of the sandwich shell $\left(\text{i.e.}, r=R_i\right)$ is subjected to a tangentially uniform moving ring heat flux. Thus, the corresponding boundary condition on this surface is as follows

$$-k\frac{\partial T}{\partial r}=q_0\,\delta\left(z-z_0(t)\right) \tag{19}$$

where q_0 and z_0 represent the intensity and the location along the *z*-axis of the moving heat flux, respectively. Also, $\delta(\ )$ is the Dirac delta function. In the current work, without losing generalization of the mathematical modelling and method of solution, the speed of the moving heat flux and mechanical loading is assumed to be a constant value *u* along the *z*-axis. These thermo-mechanical loads enter the shell at time *t*=0, when the shell is at rest and at room temperature.

The outer shell surface exchanges heat with the environment by the convection mechanism. Thus, the corresponding thermal boundary condition becomes

$$\text{At } r=R_{\text{o}}:-k\frac{\partial T}{\partial r}=h_c\left(T-T_\infty\right) \tag{20}$$

where T_∞ and h_c are the temperature of outer environment and the convective heat transfer coefficient, respectively. In comparison with the heat transfer from the lateral shell surfaces, those

at the shell ends can be ignored. Hence, the thermal boundary conditions at shell ends are simplified as

$$\text{At } z=0 \text{ and } z=L\cos\beta:\ \frac{\partial T}{\partial z}=0 \tag{21}$$

Based on the aforementioned assumptions, the corresponding initial thermal conditions become

$$T\ (r,z,0)=T_0,\ \left.\frac{\partial T\ (r,z,t)}{\partial t}\right|_{t=0}=0 \tag{22a,b}$$

Due to layerwise nature of the solution technique, the satisfaction of the thermal compatibility conditions at the interface of two neighboring layers is essential. Accordingly, the following conditions must be considered

$$T\left(R_{\mathrm{o}}^{(e)},t\right)=T\left(R_i^{(e+1)},t\right),\ k\left.\frac{\partial T}{\partial r}\right|_{r=R_o^{(e)}}=k\left.\frac{\partial T}{\partial r}\right|_{r=R_i^{(e+1)}}\quad \text{for } e=1,\ 2,\ 3 \tag{23a,b}$$

where e=1, 2 and 3 indicate the inner face sheet, the core layer and the outer face sheet layer of the sandwich shell, respectively.

The boundary conditions corresponding to a tangentially uniform moving ring pressure exerted on the shell inner surface are as follows

At $r=R_i$:

$$n_r\left[C_{11}\frac{\partial u}{\partial r}+C_{12}\frac{u}{r}+C_{13}\frac{\partial w}{\partial z}-\left(C_{11}+C_{12}+C_{13}\right)\left(\alpha\Delta T\right)\right]+n_z\left[C_{55}\left(\frac{\partial u}{\partial z}+\frac{\partial w}{\partial r}\right)\right]=P_0\,\delta\left(z-z_0(t)\right) \tag{24}$$

$$n_z\left[C_{13}\frac{\partial u}{\partial r}+C_{23}\frac{u}{r}+C_{33}\frac{\partial w}{\partial z}-\left(C_{13}+C_{23}+C_{33}\right)\left(\alpha\Delta T\right)\right]+n_r\left[C_{55}\left(\frac{\partial u}{\partial z}+\frac{\partial w}{\partial r}\right)\right]=0 \tag{25}$$

where P_0 and $z_0(t)$ are the value and the position along the z-axis of the moving pressure, respectively. The traction free boundary conditions on the shell outer surface (i.e., $r=R_{\mathrm{o}}$) are assumed. Therefore, the normal and shear components of the stress tensor must be zero on this surface

$$n_r\left[C_{11}\frac{\partial u}{\partial r}+C_{12}\frac{u}{r}+C_{13}\frac{\partial w}{\partial z}-\left(C_{11}+C_{12}+C_{13}\right)\left(\alpha\Delta T\right)\right]+n_z\left[C_{55}\left(\frac{\partial u}{\partial z}+\frac{\partial w}{\partial r}\right)\right]=0 \tag{26}$$

$$n_z\left[C_{13}\frac{\partial u}{\partial r}+C_{23}\frac{u}{r}+C_{33}\frac{\partial w}{\partial z}-\left(C_{13}+C_{23}+C_{33}\right)\left(\alpha\Delta T\right)\right]+n_r\left[C_{55}\left(\frac{\partial u}{\partial z}+\frac{\partial w}{\partial r}\right)\right]=0 \tag{27}$$

where n_r and n_z are the radial and axial components of the unit normal to the shell outer surface, respectively. In addition, the geometric and natural mechanical compatibility conditions must be kept at the interface of two adjacent shell layers "*e*" and "*e*+1"

$u\left(R_{\mathrm{o}}^{(e)},z,t\right)=u\left(R_i^{(e+1)},z,t\right),\ w\left(R_{\mathrm{o}}^{(e)},z,t\right)=w\left(R_i^{(e+1)},z,t\right)$ and

$$\left\{n_r\left[C_{11}\frac{\partial u}{\partial r}+C_{12}\frac{u}{r}+C_{13}\frac{\partial w}{\partial z}-\left(C_{11}+C_{12}+C_{13}\right)\left(\alpha\Delta T\right)\right]+n_z\left[C_{55}\left(\frac{\partial u}{\partial z}+\frac{\partial w}{\partial r}\right)\right]\right\}_{r=R_{\mathrm{o}}^{(e)}}=$$

$$\left\{n_r\left[C_{11}\frac{\partial u}{\partial r}+C_{12}\frac{u}{r}+C_{13}\frac{\partial w}{\partial z}-\left(C_{11}+C_{12}+C_{13}\right)\left(\alpha\Delta T\right)\right]+n_z\left[C_{55}\left(\frac{\partial u}{\partial z}+\frac{\partial w}{\partial r}\right)\right]\right\}_{r=R_{\mathrm{i}}^{(e+1)}},$$

$$\left\{n_z\left[C_{13}\frac{\partial u}{\partial r}+C_{23}\frac{u}{r}++C_{33}\frac{\partial w}{\partial z}-\left(C_{13}+C_{23}+C_{33}\right)\left(\alpha\Delta T\right)\right]+n_r\left[C_{55}\left(\frac{\partial u}{\partial z}+\frac{\partial w}{\partial r}\right)\right]\right\}_{r=R_{\mathrm{o}}^{(e)}}=$$

$$\left\{n_z\left[C_{13}\frac{\partial u}{\partial r}+C_{23}\frac{u}{r}++C_{33}\frac{\partial w}{\partial z}-\left(C_{13}+C_{23}+C_{33}\right)\left(\alpha\Delta T\right)\right]+n_r\left[C_{55}\left(\frac{\partial u}{\partial z}+\frac{\partial w}{\partial r}\right)\right]\right\}_{r=R_{\mathrm{i}}^{(e+1)}} \tag{28a-d}$$

where *e*=1, 2 and 3 indicate the inner face sheet, the core layer and the outer face sheet layer of the sandwich shell, respectively.

Since it is assumed that the shell is at rest before loading, the zero initial displacement and velocity are considered as the initial mechanical conditions

$$u\ \left(r,z,0\right)=0,\ w\ \left(r,z,0\right)=0,\ \left.\frac{\partial u\ \left(r,z,t\right)}{\partial t}\right|_{t=0}=0,\ \left.\frac{\partial w\ \left(r,z,t\right)}{\partial t}\right|_{t=0}=0 \tag{29a-d}$$

The shells with some combinations of the following boundary conditions at their ends are analyzed in the present work

Free (F):

$$C_{55}\left(\frac{\partial u}{\partial z}+\frac{\partial w}{\partial r}\right)=0\,,C_{13}\frac{\partial u}{\partial r}+C_{23}\frac{u}{r}+C_{33}\frac{\partial w}{\partial z}-\left(C_{13}+C_{23}+C_{33}\right)\left(\alpha\Delta T\right)=0 \tag{30a,b}$$

Simply support (S):

$$u=0\,,C_{13}\frac{\partial u}{\partial r}+C_{23}\frac{u}{r}+C_{33}\frac{\partial w}{\partial z}-\left(C_{13}+C_{23}+C_{33}\right)\left(\alpha\Delta T\right)=0 \tag{31a,b}$$

Clamped (C):

$$u=0\,,w=0 \tag{32a,b}$$

3. Method of solution

Because the presented governing differential equations have large number of variable coefficients, if it is not impossible, it would be very hard and cumbersome to solve them analytically. Therefore, the use of an appropriate approximate analytical or numerical method is essential to obtain their solution. On the other hand, it has been shown that the differential quadrature method (DQM) as an accurate and efficient numerical technique can be used for complicated structural problems; for example, see Refs. [49-53] and the related references. Therefore, this method is employed to spatially discretize the governing differential equations of each nanocomposite shell layer together with the related end boundary conditions and the compatibility conditions at the interface of two adjacent layers in the spatial domain. Since the computational domain of the DQM is a rectangular one, the skewed cross section of the multi-layered truncated conical shells must be mapped into such a domain. The transformation between the two domains is completed using the following simple geometric rules

$$r=R_2+\xi-\eta\sin\beta\,,\;z=\eta\cos\beta \tag{33}$$

where ξ and η are the coordinate variables of the computational domain (see Fig. 2). In order to reduce the mathematical manipulations and consequently computational costs, the mapping and

DQM rules are combined and the discretized equations are obtained in a single stage (see Appendix A). To start the discretization procedure of the governing differential equations and the related boundary and compatibility conditions in the computational domain, each nanocomposite layer of the sandwich shell is meshed into N_ξ and N_η discrete points along the $\xi-$ and $\eta-$ directions, respectively. At the next stage, by employing the transformed DQM rules, the thermoelastic governing differential equations and the other conditions are spatially discretized at the domain grid points and the corresponding boundary grid points, respectively. To save the paper length, only the discretized form of Eq. (16) at the domain discrete point $\left(\xi_i,\eta_j\right)$ is presented here

$$k_{ij}\left(1+\tan^2\beta\right)\sum_{k=1}^{N_\xi}B_{ik}^{\xi}T_{kj}+\left[\left(1+\tan^2\beta\right)\left(\frac{\partial k}{\partial\xi}\right)_{ij}+\frac{k_{ij}}{R_2+\xi_i-\eta_j\sin\beta}\right]\sum_{k=1}^{N_\xi}A_{ik}^{\xi}T_{kj}+k_{ij}\sec^2\beta\sum_{l=1}^{N_\eta}B_{jl}^{\eta}T_{il}+$$

$$\sec\beta\tan\beta\left(\frac{\partial k}{\partial\xi}\right)_{ij}\sum_{l=1}^{N_\eta}A_{jl}^{\eta}T_{il}+2k_{ij}\tan\beta\sec\beta\sum_{m=1}^{N_\xi}\sum_{n=1}^{N_\eta}A_{ik}^{\xi}A_{jl}^{\eta}T_{kl}=\rho_{ij}c_{ij}\left(\frac{dT_{ij}}{dt}+\tau_0\frac{d^2T_{ij}}{dt^2}\right)+$$

$$T_0\alpha_{ij}\left(3\lambda_{ij}+2\mu_{ij}\right)\left(\tau_0\frac{d^2}{dt^2}+\frac{d}{dt}\right)\left(\sum_{k=1}^{N_\xi}A_{ik}^{\xi}u_{kj}+\frac{u_{ij}}{R_2+\xi_i-\eta_j\sin\beta}+\tan\beta\sum_{k=1}^{N_\xi}A_{ik}^{\xi}w_{kj}+\right.$$

$$\left.\sec\beta\sum_{l=1}^{N_\eta}A_{jl}^{\eta}w_{il}\right) \tag{34}$$

where the DQM weighting coefficients A_{ij}^{α} and B_{ij}^{α} $\left(\alpha=\xi,\eta\right)$ are defined in Appendix A. At the end of this stage, a system of ordinary differential equations in time domain is obtained as

$$\mathbf{M}\ddot{\mathbf{d}}+\mathbf{C}\dot{\mathbf{d}}+\mathbf{K}\mathbf{d}=\mathbf{f} \tag{35}$$

where $\mathbf{d}=\left[\mathbf{T}^T\quad\hat{\mathbf{u}}^T\quad\hat{\mathbf{w}}^T\right]^T$ is the vector of unknown field variables at the grid points (or the so-called degrees of freedom vector), $\mathbf{M}$ the mass matrix, $\mathbf{C}$ the damping matrix, $\mathbf{K}$ the stiffness matrix and $\mathbf{f}$ the load vector. Vectors $\mathbf{T}$, $\hat{\mathbf{u}}$ and $\hat{\mathbf{w}}$ are the unknown temperature and displacement components vectors along the $\xi-$ and $\eta-$ axis, respectively. Also, dot over a variable or vector

means its time derivative with respect to time. It should be mentioned that based on the unknown vector definition, the elements of the matrices and the load vector in Eq. (35) are obtained from the coefficients of these field variables and the left-hand side of the discretized equations, respectively.

Different numerical techniques can be used to solve the initial value system of differential equations (35). In this work, a recently proposed multi-step method based on the NURBS curves is chosen to solve this system of equations. The computational efficiency and accuracy of this method have been successfully illustrated previously [54-58]. To apply this method, the system of equations (35) is split to a system of first-order differential equations as follows

$$\begin{cases} \dot{\mathbf{d}} = \mathbf{y} \\ \mathbf{M}\dot{\mathbf{y}} + \mathbf{C}\mathbf{y} + \mathbf{K}\mathbf{d} = \mathbf{f} \end{cases} \tag{36a,b}$$

The order of the NURBS curves and the weighting coefficients (w_i) for the NURBS curves with the same degrees are two important parameters that allow one to create different multi-step schemes. In this study, a four-step scheme with the weighting coefficients $w_1 = 10^{-3}$, $w_2 = w_1$, $w_3 = 2$ and $w_4 = 3$ [54-58] is selected to solve Eqs. (36a,b). Accordingly, the unknown variables in these equations at the time iteration "n+1" are obtained from their values at the time iterations (n,n-1,n-2,n-3) as follows, respectively

$$\begin{cases} \mathbf{d}_{n+1} = \mathbf{d}_n + \Delta t\left(a_1\mathbf{y}_n - a_2\mathbf{y}_{n-1} + a_3\mathbf{y}_{n-2} - a_4\mathbf{y}_{n-3}\right) \\ \mathbf{y}_{n+1} = \mathbf{y}_n + \Delta t\left(a_1\hat{\mathbf{y}}_n - a_2\hat{\mathbf{y}}_{n-1} + a_3\hat{\mathbf{y}}_{n-2} - a_4\hat{\mathbf{y}}_{n-3}\right) \end{cases} \tag{37a,b}$$

where

$$\hat{\mathbf{y}} = \mathbf{M}^{-1}\left(-\mathbf{C}\mathbf{y} - \mathbf{K}\mathbf{d} + \mathbf{f}\right) \tag{38}$$

$$a_1 = 1.50002585, a_2 = 0.50005291, a_3 = 2827\times10^{-8},\ a_4 = 12\times10^{-7} \tag{39a-d}$$

Also, Δt is the time step size.

It should be mentioned that in using this approach, the strong forms of the boundary conditions are also exactly discretized at the boundary grid points by employing the DQM rules. Then, the results are considered as algebraic equations into the final system of algebraic equations resulted from the differential equations governing the thermoelastic behavior of the shell under investigation. In addition, any types of boundary conditions can be easily implemented.

The solution process is started by determining the values of the unknown field variables at the first four points using the initial conditions and by solving a system of linear algebraic equations resulted from the first, second and third multi-step schemes. Afterward, the values of unknown field variables at the next iteration are determined. More details of this procedure can be found in Ref. [54]. The obtained results are then used as the initial conditions for the next time step. Finally, the output of this technique is the time history of the thermoelastic field variables at the DQ grid points of each GPLRC shell layer.

4. Numerical results

In this section, at first the current approach is validated and then some new numerical results are presented and discussed. The matrix phase of the sandwich shell is assumed to be epoxy and its material properties together with those of the reinforcing phase (i.e., GPLs) are provided in Table 1. If otherwise not stated, the following non-dimensional parameters are used to facilitate the parametric studies

$$Fo=\frac{tu^{*}}{L},\ \tau=\sqrt{\frac{\tau_0\hat{\alpha}}{R_{\mathrm{m}}^{2}}},\ T^{*}=\frac{h_c L^{2}}{q_0 h^{2}}T,\ U=\frac{u}{\left(1+\nu_{GPL}\right)R_{\mathrm{m}}\alpha_{GPL}T_{\infty}},\ \zeta=\frac{\xi}{b},\ \Sigma_{ij}=\frac{\left(1+\nu_{GPL}\right)}{E_{GPL}\alpha_{GPL}T_{\infty}}\sigma_{ij} \quad \text{(40a-f)}$$

where $\hat{\alpha}\left(=k/\rho c\right)$ is the thermal diffusivity of the sandwich shells. In the absence of other specifications, the GPLs dimensions [41] and the other geometrical and physical parameters of the FG-GPLRC shells are assumed to have the following values

$a_{GPL}=2.5(\mu\mathrm{m}),\quad b_{GPL}=1.5(\mu\mathrm{m}),\quad t_{GPL}=1.5(\mathrm{nm}),\quad R_m=1(\mathrm{m}),\quad L=1(\mathrm{m}),\quad h=0.1(\mathrm{m}),$
$q_0=50000(\mathrm{W/m^2}),T_0=T_\infty=300(\mathrm{K}),\ h_c=100\,(\mathrm{W/m^2K}),\ \gamma=0.5,\ P_0=100\,(\mathrm{MPa}).$
Also, in this section, the symbolism such as "C-F", means that the edge z=0 is clamped and the edge z=L has free boundary conditions.

4.1. Validation

As a first example, comparison between the results when using the NURBS-based multi-step time integration scheme and the Galerkin scheme from the Newmark's family of time integrations is executed to verify its superior computational efficiency over this conventional approach. In this regard, the data in Table 2 show the convergence rate and the CPU time requirements of both methods for the thermoelastic analysis of the multilayer truncated conical shells with the GPLRC-FS and GPLR-PC subjected to thermo-mechanical moving loads. The non-dimensional displacement and temperature at points $\varsigma=0$ are provided in this table. Based on the presented results, it is noted that in spite of the close agreement between the converged results of the two methods, the CPU time requirement of NURBS-based multi-step technique is much less than that of the Newmark's scheme.

The convergence behaviors of the non-dimensional thermoelastic field variables of the multilayer truncated conical shell with the GPLRC-FS and GPLRC-PC under the thermomechanical loadings against the DQ number of grid points along the radial and axial directions are exhibited in Figs. 3 and 4, respectively. As depicted in these figures, seven grid points per layer in the radial direction $(N_\xi=7)$ and twenty-nine grid points along the axial direction $(N_\eta=29)$ yield adequate results. Also, based on the convergence study performed in Table 2, 400 time steps are used to solve the system of ordinary differential equations (36) in the temporal domain.

To validate the presented approach for the thermoelastic analysis of rotating the FG truncated conical shell, an FG annular disk, as a limiting case of a truncated conical shell (truncated conical shell with $\beta = \pi/2$ and small length-to-outer radius ratio), subjected to a thermal environment studied by Peng and Li [59] using an analytical solution is analyzed here. Peng and Li [59] transformed the one-dimensional thermoelasticity equation into a Fredholm integral equation to obtain the analytical solution. To find such a solution, all the material properties, except Poisson's ratio, were assumed to vary according to $\psi = \psi_0 r^n$ where ψ_0 is a material constant at the outer surface and *n* is the material graded index. The material properties are as follows [59],

$$E_m = 70\,\text{GPa},\ \nu_m = 0.3,\ K_m = 209\left(\text{W/m}^\circ\text{C}\right),\ \alpha_m = 23\times10^{-6}\left(1/^\circ\text{C}\right),\ \rho_m = 2700\left(\text{Kg/m}^3\right),$$

$$E_c = 151\,\text{GPa},\ \nu_c = 0.3,\ K_c = 2\left(\text{W/m}^\circ\text{C}\right),\ \alpha_c = 10\times10^{-6}\left(1/^\circ\text{C}\right),\ \rho_c = 5700\left(\text{Kg/m}^3\right),$$

Also the surface temperature at the inner and outer surfaces of the disk is assumed to be

$$T\left(R_i\right) = 0\ ^\circ C,\ T\left(R_o\right) = 1000\ ^\circ C \tag{41a, b}$$

where R_i and R_o are inner and outer radius of disk, respectively.

The non-dimensional radial displacement and the non-dimensional radial and tangential stress components at different locations and for different values of the material graded index (n) are compared with those of Peng and Li [59] in Table 3. Excellent agreement between the results of the two approaches can be seen.

For further validation of the present approach, the thermoelastic analysis of FG hollow cylindrical shells subjected to a thermal loading available in the literature is conducted. For this purpose, the formulation degenerates to those of the cylindrical shells by setting $\beta = 0$. This example is chosen from the work of Santos et al. [60], who analyzed the FG cylindrical shells under thermal loading in the context of the uncoupled thermoelasticity. The material properties of the

shell constituents are provided in Table 4. They presented a semi-analytical finite element solution for the FG cylindrical shells subjected to the following thermal boundary and initial conditions

$$\text{At } r = R_i: \; T(r,z,t) = T_0\left(1 - e^{-0.5t}\right) \tag{42}$$

$$\text{At } r = R_o: \; k\frac{\partial T}{\partial r} + h_c T = 0 \tag{43}$$

$$\text{At } z = 0, L: T(r,z,t) = 0 \tag{44a,b}$$

They assumed that the material composition changes across the shell thickness from ceramic at the inner surface to metal at the outer surface along with the power law distribution as

$$P(r) = P_c + (P_m - P_c)V_m \tag{45}$$

where P is a generic material property, and $V_m = \left(\frac{r - R_i}{R_o - R_i}\right)^p$ is the volume fraction of metal phase, wherein p denotes the power law index. In Figs. 5 (a) and (b), the through-the-thickness non-dimensional temperature and displacement variations according to the two approaches and for different values of the power law index p are compared. The excellent agreement between the results of the two approaches shows the accuracy of the present approach.

The present approach is further validated by analyzing an elastodynamic problem of FG truncated conical shells. For this purpose, the free vibration frequencies of a FG truncated conical shell with fully clamped ends are determined and compared with those reported by Bhangale et al. [61]. They estimated the frequencies based on the FSDT of shells by employing the finite element method. In their work, all the material properties vary according to the power law distribution as presented in Eq. (45) with $V_m = 1 - \left(\frac{2z + h}{2z}\right)^p$. Also, the following values for the material properties of the metal (SUS304) and ceramic (Si3N4) phases are considered

$E_m = 322.27\,\text{GPa}, \nu_m = 0.24, \rho_m = 2370\left(\text{kg/m}^3\right); E_c = 207.7877\,\text{GPa}, \nu_c = 0.317756,$

$\rho_c = 8166\left(\text{kg/m}^3\right)$

In Figs. 6 (a) and (b) for two different values of the semi-vertex angle and the power law index p, the frequencies of the first 20 circumferential modes of the shell are illustrated and compared with those provided in Ref. [61]. The consistence between the obtained frequencies and those of Ref. [61] partially verifies the current approach.

4.2. Parametric studies

In this section, some parametric studies aim at analyzing the sensitivity of the responses to different porosity distribution and amount, GPLs weight fraction, boundary conditions at the shell ends, moving thermomechanical load velocity, etc.

As the first study, the effects of the porosity distribution on the through-the-thickness variations and the time-histories of the no-dimensional temperature, displacement and stress tensor components of the sandwich shells under investigation are exhibited in Figs. 7 and 8, respectively. As can be observed from Figs. (7a) the gradient of the temperature in the type-2 shell of the porosity distribution is greater than those of the other cases when ξ lies between 0 and almost 0.3. In addition, the displacement gradient of this type of shell is generally greater than those of the other two shell types of the porosity distributions. These issues together with the nonlinear variations of the material properties along the thickness direction cause a different trend of the stress variations for the type-2 shell in comparison with the other two cases. The influences of the porosity amount on these non-dimensional field variables are shown in Figs. 9 and 10 and Table 5. The results in these figures and table indicate that both the porosity distribution and porosity amount change the temperature distribution in the region traveled by the heat wave. However, they have no visible effect on the time histories of temperature at a specified point of the shell. This is because the

nonuniform distribution of the porosities in the core thickness direction causes the thermal properties to vary in this direction. Thus, by changing the type of porosity distribution, the variations of these parameters change, and the temperature distribution in the thickness direction also changes. However, since the porosity distribution and amount do not significantly affect the thermal properties of the sandwich shell under consideration, the time history of temperature at a specific point of the shell does not change considerably. For example, the variations in the specific heat capacity, thermal conductivity and mass density of the shell are smaller than 2 percent once the porosity amount parameter (i.e., e_0) increases from 0 to 0.6. On the other hand, its effects on the Young's modulus of the sandwich shell are excessive. The Young's modulus of the shell is reduced by almost 37.46% when the porosity amount changes from 0 to 0.6. Thus, by increasing the porosity amount parameter (i.e., e_0), the overall stiffness of the shell reduces, which increases the displacement components. In addition, any porosity distribution that reduces the overall stiffness of the shell, increases the displacement components. Among the three types of porosity distributions considered in this work, more porosities are distributed in the region near the inner surface of the core layer in type-3 distribution, whereas more porosities are distributed near the inner and outer surfaces of the core layer in type 2, and near the middle region of the core layer in type 1. On the other hand, it can be realized that the more away the porosity distribution from the outer surface of the core layer, the stiffer the shell structure. It can be seen that the stress components are affected by the type of porosity distribution and amount. This is because the variations of the porosity distribution in the core layer cause the variation of the shell Young's modulus in the shell thickness direction and the increase of the porosity amount further increases the variation of the material properties. It should be noted that if the Young's modulus remains constant, its constant value does not affect the stress tensor components in the shell layers. Thus,

both the porosity distribution type and amount affect the stress tensor components in the shell layers, and a stiffer shell has lower stress components in general. The obtained results confirm this behavior, further validating the present approach. In addition, one can see that the stress components approach their steady state values when the time level increases.

To explore the effects of GPLs weight fraction on the thermoelastic characteristics of the sandwich truncated conical shells, the through-the-thickness variations of dimensionless temperature, radial displacement and stress components are illustrated in Fig. 11, and the time histories of these filed variables at the points on the centerline of the shell middle section are shown in Fig. 12. As can be seen from Fig. 11(a), by increasing the GPL weight fraction, the heat wave speed increases meanwhile the maximum temperature decreases (see also Fig. 12(a)). The reason of this is that by adding GPLs, the thermal conductivity increases noticeably, but the density and specific heat capacity reduce a little. On the other hand, from Eq. (16), it can be deduced that the heat wave speed is proportional to $\sqrt{\frac{k}{\rho c \tau_0}}$. Therefore, any parameter that increases the thermal conductivity and decreases the mass density and specific heat capacity will increase the heat wave speed. In addition, when the GPLs weight fraction increases from zero to one percent, the thermal conductivity is increased by 78%, meanwhile the mass density and specific heat capacity have no considerable change and virtually remain constant. As a results, the maximum temperature must decrease by increasing the GPLs weight fraction. Figs. 11 (b) and (12b) depict the influences of GPLs weight fraction on the dimensionless radial displacement component. It is clear from Fig. 11 (b) that by increasing the GPL weight fraction, the distribution of the displacement component changes. Since the GPLs are uniformly distributed, the change of the weight fraction should not affect the distribution of the displacement component and therefore, there must be other reasons for this trend. One of the major features in this regard may be due to the dissimilar boundary conditions on the inner and outer surfaces of the shell. To further discuss this issue, it should be noted that the outer surface of the shell is traction free meanwhile its inner surface is subjected to a thermomechanical moving load. Thus, the boundary conditions on the outer surface become independent of the Young's modulus, and the boundary conditions on its inner surface depend on it (see Eq. (24)). In addition, the boundary conditions at the ends of the shell are independent of the

Young's modulus. Thus, by changing the Young's modulus, the displacement variation along the radial direction should change. Also, another feature that could affect this issue slightly is the variation of temperature distribution due to change of the GPLs weight fraction. The reduction of the displacement at all times when the load is applied on the shell is more exhibited in Fig. 12 (b). The reason of this trend is that by increasing the GPL weight fraction, the overall shell stiffness increases and consequently, the displacement decreases. As can be expected, the change of the GPL weigh fraction does not affect the distributions of the stress components along the radial direction. This is owing to two reasons: 1) the uniform distribution of the GPLs through the thickness of the shell, 2) the linear analysis of the shell deformation, which make the stress components independent of the change of the Young's modulus. The same behavior is observed for the time histories of the stress components in Figs. 12 (c) and (d), except when the load is at the near- end of the shell for the relatively large value of GPLs weight fraction which may be computational error due to very low values of the stress components. These expectations validate the reported results.

The effects of dimensionless relaxation time on the temperature and displacement variations along the shell thickness for two different positions of the thermo-mechanical loading are illustrated in Fig. 13. It is clear that by increasing the relaxation time, the temperature rise decreases. This is due to the fact that by increasing this parameter the heat wave speed $\left(\sqrt{\frac{k}{\rho c \tau_0}}\right)$ decreases. When the load is at middle section of the shell (i.e., the case of F_o=0.5), neither the displacement nor the temperature is considerably changed by varying the dimensionless relaxation time. But, when the load leaves the shell (i.e., the case of F_o=1.0), its effects on the reduction of temperature and displacement are clearly observable.

The impacts of thermo-mechanical moving load speed on the thermoelastic responses of the sandwich truncated conical shell with the GPLRC-FS and GPLRC-PC are studied in Figs. 14 and 15. These figures show that the temperature and displacement decrease when increasing the thermo-mechanical load speed in the range of 0.01 to 1 (cm/s). This is because by increasing the load speed, the time duration of the applied moving load reduces and also the load travels through the shell in less time. Due to its thermal resistance and inertia, the shell cannot react to this rapidly-applied load promptly, and therefore, the temperature and displacement reduce by increasing the

moving load speed. On the other hand, when increasing the load speed, the gradient of the displacement decreases, which causes the reduction of the strain components and consequently the stress components as observed in Figs. 14(c), 14 (d),15 (c) and 15 (d).

The influences of the shell thickness-to-length ratio on the thermoelastic behavior of the sandwich shell under investigation are shown in Figs. 16 and 17. It is observed that the increase of this geometric parameter causes the reduction of the temperature, displacement and stress components. This is because, by increasing the shell thickness, the thermal resistance, the mass and the overall stiffness of the sandwich shell increase, which reduces the transient temperature and the displacements of the shell when it is subjected to a constant moving internal heat flux and ring pressure. In addition, the increase of the shell thickness reduces the displacement gradients, consequently decreasing the values of stress components. It is interesting to note that by increasing the shell thickness the heat wave front becomes observable.

In Figs. 18-20, the impacts of different end boundary conditions of the shell on its dimensionless displacement and stress components are explored. The through-the-thickness variations of the dimensionless field variables at two dimensionless times F_o=0.5 and F_o=1 are shown in Figs. 18 and 19, respectively. When F_o=0.5, the load is at the middle section of the shell, and when F_o=1, the load is at the end section of the shell. It is observed that the influences of the boundary conditions on the responses of the shell depend on the location of the load. However, the shell with completely clamped edges has the lowest displacement and stress values regardless of the load position. When the load is at the middle section of the shell, the stress components of the shell with the C-S ends have slightly greater magnitudes than those of the shell with C-F ends. This is because in this situation, the displacement gradients of the shell with C-S ends are greater than those of the shell with a free edge. But when F_o=1.0, the load is on the end section of the shell and it can be expected, the shell with C-F edges has the greatest displacement and stress components in this case. At this time, the load acts on the free edge of the shell with C-F ends and on the simply supported edges of the shell with C-S ends. On the other hand, the simply supported and clamped constraints prevent the radial displacement of edges. Thus, less deformations are induced for the shells with C-C and C-S edges than the shell with C-F edges at this position. Also, based on Fig. 19, there are no substantial differences between the results through the thickness direction for the shells with C-F and C-S edges. The time histories of the dimensionless displacement and stress components at the points on the center of the middle section of the shell are exhibited in Fig. 20. The results show

that by increasing the constraints at the edges of the shell, the dimensionless displacement and hoop stress component reduce. Due to one free edge, the shell with C-F edges can more easily expand in the radial direction under the internally applied load than the shells with C-C and C-S edges. Thus, it has greater hoop stresses than those of the shells with the other boundary conditions. As can be expected, the maximum transverse shear stress component $\left(\Sigma_{rz}\right)$ and the axial stress component $\left(\Sigma_{zz}\right)$ of the shell with C-F boundary conditions are lower than those of the shells with C-C and C-S boundary conditions. This is owing to the fact that to prevent the radial displacement of the shell edges, the nonzero transverse shear stresses must exist at these edges. For the shell with one free edge, the transverse shear stress is absent on the free edge and consequently, the maximum value of this stress component becomes less than those of the other cases. However, at the time that the thermo-mechanical load is near the end of the shell, due to the radial edge constraints the shell with C-C and C-S edges have lower transverse shear and axial normal stress components than the shell with C-F edges.

5. Conclusions

The thermoelastic responses of the sandwich truncated conical shells with GPLRC face sheets and GPLRC porous core subjected to moving thermo-mechanical load were investigated successfully based on the Lord-Shulman thermoelasticity theory. The applied theory had no kinematical assumption as those used in the two-dimensional theories, thus accurately predicted the thermoelastic behaviors of the sandwich truncated conical shells. On the other hand, the numerical method employed to obtain the solution was a layerwise hybrid technique that used the strong form of the equations, and also implemented the boundary and compatibility conditions at the interfaces of the layers exactly at the corresponding grid points. Also, the time domain was discretized using a computationally efficient multi-step NURBS based technique. After verifying the correctness and accuracy of the proposed approach in the limit cases, some parametric studies were conducted and discussed to explore the effects of the porosity distribution and amount, GPLs weight fraction, load velocity, edge boundary conditions and the shell geometric parameters on the thermoelastic behaviors of the under-investigation sandwich shells. Based on the provided results, some findings are summarized as follows:

- The porosity distribution and amount do not significantly affect the time history of temperature at a specific point of the shell; however, they change the distribution of temperature along the thickness direction.
- The increase of porosity amount increases the displacement components. In addition, the type of porosity distribution affects the displacement, and in the case when the porosities are more distributed near the inner surface of the core layer, the displacement has the lowest values.
- The increase of the GPLs weight fraction increases the heat wave speed but decreases the maximum value of the temperature.
- The GPLs weigh fraction has no influence on the stress components, but addition of GPLs reduces the displacement component considerably. In addition, the increase of the GPLs weight fraction changes the distribution of the radial displacement component along the shell thickness direction.
- By increasing the thickness-to-length of the shell, the temperature, displacement and stress components reduce.
- The impacts of the end boundary conditions of the shell on its response depend on the position of the moving thermo-mechanical load. However, the shell with completely clamped edges has the lowest displacement and stress values regardless of the load position in comparison with the C-F and C-S ends shells.

In the future works, the influences of the geometric nonlinearity on the thermoelastic responses of the sandwich shells with GPLs with GPLs reinforced face sheets and porous core subjected to different moving thermo-mechanical loads will be studied.

Appendix A. The combined geometric mapping and DQM

Using the geometric transformation together with the DQM rules, the spatial derivatives are discretized as [41]

$$\left.\frac{\partial u}{\partial r}\right|_{(r_i,z_j)}=\sum_{m=1}^{N_\xi}A_{im}^{\xi}u_{mj}\ ,\ \left.\frac{\partial u}{\partial z}\right|_{(r_i,z_j)}=\tan\beta\sum_{m=1}^{N_\xi}A_{im}^{\xi}u_{mj}+\sec\beta\sum_{n=1}^{N_\eta}A_{jn}^{\eta}u_{in}\ ,\ \left.\frac{\partial^2 u}{\partial r^2}\right|_{(r_i,z_j)}=\sum_{m=1}^{N_\xi}B_{im}^{\xi}u_{mj}$$

$$\left.\frac{\partial^2 u}{\partial z^2}\right|_{(r_i,z_j)}=\tan^2\beta\sum_{m=1}^{N_\xi}B_{im}^{\xi}u_{mj}+\sec^2\beta\sum_{n=1}^{N_\eta}B_{jn}^{\eta}u_{in}+2\sec\beta\tan\beta\sum_{m=1}^{N_\xi}\sum_{n=1}^{N_\eta}A_{im}^{\xi}A_{jn}^{\eta}u_{mn}$$

$$\left.\frac{\partial^2 u}{\partial r \partial z}\right|_{(r_i, z_j)} = \tan\beta \sum_{m=1}^{N_\xi} B_{im}^{\xi} u_{mj} + \sec\beta \sum_{m=1}^{N_\xi} \sum_{n=1}^{N_\eta} A_{im}^{\xi} A_{jn}^{\eta} u_{mn} \quad \text{(A1-5)}$$

where A_{ij}^{α} and B_{ij}^{α} $(\alpha = \xi, \eta)$ are the DQM weighting coefficients of the first and second-order derivatives in the α-direction, respectively [41]. Also,

$$r = R_2 + \zeta - \eta \sin\beta\,,\ z = \eta\cos\beta \quad \text{(A6,7)}$$

Nomenclature

$A_{ij}^{\xi}, A_{ij}^{\eta}$	The DQM first-order weighting coefficients corresponding to the $\xi-$ and $\eta-$directions, respectively, m^{-2}
a_{GPL}	The GPLs length, m
b_{GPL}	The GPLs width, m
$B_{ij}^{\xi}, B_{ij}^{\eta}$	The DQM second-order weighting coefficients corresponding to the $\xi-$ and $\eta-$directions, respectively, m^{-4}
b	The total thickness of the truncated cone in the computational domain, m
c	The specific heat capacity, $J.kg^{-1}.K^{-1}$
c_{ij}	The specific heat capacity at a typical grid point (ξ_i, η_j), $J.kg^{-1}.K^{-1}$
C_{ij}	The material stiffnesses at a typical grid point (ξ_i, η_j), $N.m^{-2}$
C	The damping matrix
Δt	Time step, s
E	The effective Young's modulus, $N.m^{-2}$

e_0, e_m	The porosity coefficients, dimensionless
Fo	Fourier number, dimensionless
f	The load vector
$H(p)$	A geometric parameter, dimensionless
h	The thickness of the truncated cone in each layer, m
h_c	The convective heat transfer coefficient, $W.m^{-2}.K$
k	The thermal conductivity, $W.m^{-1}.K^{-1}$
k_{GPL}	The thermal conductivity of the GPLs, $W.m^{-1}.K^{-1}$
k_{ij}	The thermal conductivity at a typical grid point (ξ_i, η_j), $W.m^{-1}.K^{-1}$
k_m	The thermal conductivity of the matrix, $W.m^{-1}.K^{-1}$
K	The stiffness matrix
L	Length of the truncated cone, m
M	The mass matrix
m	The material graded index, dimensionless
N_L	The number of physical layers
N_t	The number of time steps, dimensionless
N_ξ, N_η	The grid points along the ξ , η and θ-directions, dimensionless
P	A typical material property
p	The power law index, dimensionless
P_o	The value of the moving pressure, $N.m^{-2}$
q_0	The intensity of the moving heat flux, $J.m^{-2}.s^{-1}$

R_i, R_o	The inner and outer radius of the shell, m
$R_i(z)$, $R_o(z)$	The inner and outer radiuses of the truncated cone at the section z, m
R_1, R_2	The inner radiuses of the largest and smallest sections of the truncated cone, m
R_m	The mean radius of the truncated cone at section $L\cos\beta/2$, m
r	The radial coordinate variable, m
T	Temperature, K
T_{ij}	The temperature at a typical grid point (ξ_i, η_j), K
T_0	The initial temperature, K
$\mathbf{T}$	The unknown temperature vector
T_∞	The ambient temperature, K
$\overline{T}$, T^*	The non-dimensional temperature, dimensionless
t	Time, s
t_{GPL}	The GPLs thickness, m
n_r , n_z	The radial and axial components of the unit normal to the shell outer surface, dimensionless
U	A dimensionless parameter, defined in equation (40d)
u	The displacement component along the radial direction, m
$\hat{\mathbf{u}}$	The unknown displacement components vector along the $\xi-$axis
u^*	The velocity of the moving load, cm.s^{-1}
V_{GPL}	The GPLs volume fraction, dimensionless
V_m	The matrix volume fraction, dimensionless
w	The displacement component along the axial direction, m

$\hat{\mathbf{w}}$	The unknown displacement component vector along the $\eta-$axis, m
w_{GPL}	The GPLs weight fraction, dimensionless
w_i	The weighting coefficients of the multi-step time integration scheme, dimensionless
z	The axial coordinate variable, m
z_o	The location of the thermomechanical moving load along the z-axis, m

Greek symbols

α	The thermal expansion coefficient, K^{-1}
α_{ij}	The thermal expansion coefficient at a typical grid point (ξ_i,η_j), K^{-1}
β	The semi-vertex angle, degree
γ	A fitting parameter, dimensionless
ζ	A dimensionless parameter, defined in equation (40e)
η	A coordinate variable in the computational domain, m
θ	A cylindrical coordinate variable, degree
Σ_{ij}	A dimensionless parameter, defined in equation (40f)
σ_{ij}	The stress tensor components, $N.m^{-2}$
ε_{ij}	The strain tensor components, dimensionless
λ and μ	The Lamé's elastic constants, $N.m^{-2}$
ν	The poisson's ratio, dimensionless
ξ	The coordinate variable in the computational domain, m
ρ	Density, $kg.m^{-3}$
ρ_{ij}	The density at a typical grid point (ξ_i,η_j), $kg.m^{-3}$

τ_0	The relaxation time, s
τ	A dimensionless parameter, defined in equation (40b)
Ξ	The porosity function
$\delta(\quad)$	Dirac delta function

Subscripts

c	Ceramic material
GPL	Graphene platelets
m	Matrix material
i	Grid point along the ξ-direction
j	Grid point along the η-direction
χ	The porosity coefficient

Superscripts

e	Physical layer
N_L	Outer layer
p	Power law index, dimensionless
$-$	Dimensionless
$*$	Dimensionless

References

1. Sofiyev AH. Review of research on the vibration and buckling of the FGM conical shells. Compos Struct 2019;211:301-317. https://doi.org/10.1016/j.compstruct.2018.12.047.

2. Duc ND, Kim SE, Chan DQ. Thermal buckling analysis of FGM sandwich truncated conical shells reinforced by FGM stiffeners resting on elastic foundations using FSDT. J Thermal Stresse 2018;41(3):331-365. https://doi.org/10.1080/01495739.2017.1398623.
3. Manh DT, Anh VTT, Nguyen PD, Duc ND. Nonlinear post-buckling of CNTs reinforced sandwich-structured composite annular spherical shells. Int J Struct Stab Dy 2020; 20: 2050018. https://dx.doi.org/10.1142/S0219455420500182.
4. Avey M, Fantuzzi N, Sofiyev AH. Mathematical modeling and analytical solution of thermoelastic stability problem of functionally graded nanocomposite cylinders within different theories. Mathematics 2022;10(7):1081. https://doi.org/10.3390/math10071081.
5. Avey M, Aslanova N, Sofiyev AH. Modeling and solution of the buckling problem of axially loaded laminated nanocomposite truncated conical shells in thermal environments. ZAMM – J Appl Math Mech 2025;105 (2): 1-25, e202401190. https://doi.org/10.1002/zamm.202401190.
6. Tan NC, Dzung NM, Ha NH, Tien ND, Hung NC, Sofiyev AH, Ninh DG. Novel sandwich composite shell structures in nonlinear geometric and dynamic analyses. AIAA J 2025; 1-24. https://doi.org/10.2514/1.J065315.
7. Hong C-C. Thermal vibration of thick FGM conical shells by using third-order shear deformation theory. Materials 2024;17(10): 2403. https://doi.org/10.3390/ma17102403.
8. Gao Z, Shi X, Huang Z, Zhong R, Wang Q. Spectro-geometric solutions for random vibration of functionally graded graphene platelet reinforced conical shells. Thin-Wall Struct 2024; 195: 111410. https://doi.org/10.1016/j.tws.2023.111410.
9. Khorasani M, Soleimani-Javid Z, Arshid E, Lampani L, Civalek Ö. Thermo-elastic buckling of honeycomb micro plates integrated with FG-GNPs reinforced Epoxy skins with stretching effect. Compos Struct 2021;258:113430. https://doi.org/10.1016/j.compstruct.2020.113430.
10. Arefi M, Kiani Moghaddam S, Mohammad-Rezaei Bidgoli E, Kiani M, Civalek O. Analysis of graphene nanoplatelet reinforced cylindrical shell subjected to thermo-mechanical loads. Compos Struct 2021;255:112924. https://doi.org/10.1016/j.compstruct.2020.112924.
11. Sobhan E, Masoodi AR, Civalek O, Ahmadi-Pari AR. Agglomerated impact of CNT vs. GNP nanofillers on hybridization of polymer matrix for vibration of coupled hemispherical-conical-conical shells. Aerosp Sci Technol 2022;120: 107257. https://doi.org/10.1016/j.ast.2021.107257.

12. Liang Y, Zheng S, Wang H, Chen D. Nonlinear isogeometric analysis of axially functionally graded graphene platelet-reinforced composite curved beams. Compos Struct 2024;330:117871. https://doi.org/10.1016/j.compstruct.2023.117871.
13. Dutta T, Llamas-Garro I, Velázquez-González JS, Bas J, Dubey R, Mishra SK. A new generation of satellite sensors based on graphene and carbon nanotubes: A Review. IEEE Sens J 2024;24:31645-31657. doi: 10.1109/JSEN.2024.3440499.
14. Hussain M, Khan SM, Shafiq M, Al-Dossari M, Alqsair UF, Khan SU, Khan MI. Comparative study of PLA composites reinforced with graphene nanoplatelets, graphene oxides, and carbon nanotubes: Mechanical and degradation evaluation. Energy 2024;308:132917. https://doi.org/10.1016/j.energy.2024.132917.
15. Shi G, Araby S, Gibson CT, Meng Q, Zhu S, Ma J. Graphene platelets and their polymer composites: Fabrication, structure, properties, and applications. Adv Funct Mater 2018;28(19):1706705. https://doi.org/10.1002/adfm.201706705.
16. Qi P, Chen X, Zhu H, Lyu Y, Zhang B, Peng Q, Feng X, Fan T, Zhang D. Quantifying the effects of geometric parameters on the elastic properties of multilayer graphene platelet films, Adv Mater 2025; 2502546. https://doi.org/10.1002/adma.202502546.
17. Mousavi SR, Estaji S, Kiaei H, Mansourian-Tabaei M, Nouranian S, Jafari SH, Ruckdäschel H, Arjmand M, Khonakdar HA. A review of electrical and thermal conductivities of epoxy resin systems reinforced with carbon nanotubes and graphene-based nanoparticles. Polym Test 2022;112:107645. https://doi.org/10.1016/j.polymertesting.2022.107645.
18. You X, Zhang Q, Yang J, Dong S. Review on 3D-printed graphene-reinforced composites for structural applications. Compos Part A-Appl S 2023;167:107420. https://doi.org/10.1016/j.compositesa.2022.107420.
19. Yee K, Ghayesh MH. A review on the mechanics of graphene nanoplatelets reinforced structures. Int J Eng Sci 2023;186:103831. https://doi.org/10.1016/j.ijengsci.2023.103831.
20. Barbaros I, Yang Y, Safaei B, Yang Z, Qin Z, Asmael M. State-of-the-art review of fabrication, application, and mechanical properties of functionally graded porous nanocomposite materials. Nanotechnol Rev 2022;11 (1):321-371. https://doi.org/10.1515/ntrev-2022-0017.

21. Chen D, Gao K, Yang J, Zhang L. Functionally graded porous structures: Analyses, performances, and applications-a review. Thin-Walled Struct 2023;191:111046. https://doi.org/10.1016/j.tws.2023.111046.
22. Liu T, Sun X, Hu WF, Wang L, Zhang S, Bui TQ. Nonlinear thermal-mechanical coupled isogeometric analysis for GPLs reinforced functionally graded porous plates. Eng Struct 2024;319:118827. https://doi.org/10.1016/j.engstruct.2024.118827.
23. Zhu J, Wang Z, Zhang L, Wu H, Zhao L, Zhang H, Wu H. Wave propagation in the semi-infinite functionally graded porous plates reinforced with graphene platelets. Int J Struct Stab Dy 2024;24(21): 2450245. https://doi.org/10.1142/S0219455424502456.
24. Duc ND, Cong PH, Tuan ND, Phuong Thanh Tran NV. Thermal and mechanical stability of functionally graded carbon nanotubes (FG CNT)-reinforced composite truncated conical shells surrounded by the elastic foundations. Thin-Walled Struct 2017; 115: 300-310. https://doi.org/10.1016/j.tws.2017.02.016.
25. Chan DQ, Quan TQ, Kim SE, Duc ND. Nonlinear dynamic response and vibration of shear deformable piezoelectric functionally graded truncated conical panel in thermal environments. Eur J Mech A-Solid 2019; 77: 103795. https://doi.org/10.1016/j.euromechsol.2019.103795.
26. Chan DQ, Anh VTT, Duc ND. Vibration and nonlinear dynamic response of eccentrically stiffened functionally graded composite truncated conical shells in thermal environments. Acta Mech 2019; 230: 157-178. https://doi.org/10.1007/s00707-018-2282-4.
27. Chan DQ, Long VD, Duc ND. Nonlinear buckling and post-buckling of FGM shear deformable truncated conical shells reinforced by FGM stiffeners. Mech Compos Mater 2019; 54 (6): 754-764. https://doi.org/10.1007/s11029-019-9780-x.
28. Chan DQ, Thanh NV, Khoa ND, Duc ND. Nonlinear dynamic analysis of piezoelectric functionally graded porous truncated conical panel in thermal environments. Thin Walled Struct 2020; 154: 106837. https://doi.org/10.1016/j.tws.2020.106837.
29. Duc ND, Quan TQ, Cong PH. Nonlinear vibration of auxetic plates and shells. Vietnam National University Press, Hanoi, 2021.
30. Yang S, Hao Y, Zhang W, Yang L, Liu L. Nonlinear vibration of functionally graded graphene platelet reinforced composite truncated conical shell using first-order shear deformation theory. Appl Math Mech -Engl Ed 2021;42(7):981–998. https://doi.org/10.1007/s10483-021-2747-9.

31. Bahranifard F, Malekzadeh P, Golbahar Haghighi MR, Malakouti M. Free vibration of point supported ring-stiffened truncated conical sandwich shells with GPLRC porous core and face sheets. Mech Based Des Struc 2024;52:6142-6172. https://doi.org/10.1080/15397734.2023.2272674.
32. Youseftabar H, Hosseinnejad F, Rostamiyan Y, Seyyedi SM, Rabbani M. Effect of porosity on the nonlinear free vibrational behavior of two-directional functionally graded porous cone-shaped shells resting on elastic substrates. Mech Based Des Struc 2024;52:8544-8566. https://doi.org/10.1080/15397734.2024.2323147.
33. Li H, Zhang W, Zhang YF, Jiang Y. Nonlinear vibrations of graphene-reinforced porous rotating conical shell with arbitrary boundary conditions using traveling wave vibration analysis. Nonlinear Dyn 2024;112:4363–4391. https://doi.org/10.1007/s11071-023-09255-3.
34. Huang XL, Wei Y, Mo W, Zhang Y. Nonlinear Vibration Analysis of Axially Moving Truncated Porous Composite Conical Shells Reinforced with Graphene Nanoplatelets. J Vib Eng Technol 2025;13:121. https://doi.org/10.1007/s42417-024-01626-3.
35. Khoddami Maraghi Z, Safari I, Ghorbanpour Arani A, Shekari AM, Saeidnejad S, Zahedi Bidgoli A. Free vibration analysis of sandwich graphene-reinforced nanocomposite truncated conical shells with auxetic honeycomb core. J Strain Anal Eng Des 2025, https://doi.org/10.1177/03093247241311.
36. Huang XL, Mo W, Sun W, Xiao W. Buckling analysis of porous functionally graded GPL-reinforced conical shells subjected to combined forces. Arch Appl Mech 2024;94:299–313. https://doi.org/10.1007/s00419-023-02521-1.
37. Bahranifard F, Malekzadeh P, Golbahar Haghighi MR. Moving load response of ring-stiffened sandwich truncated conical shells with GPLRC face sheets and porous core. Thin-Walled Struct 2022;180:109984. https://doi.org/10.1016/j.tws.2022.109984.
38. Bahranifard F, Malekzadeh P, Golbahar Haghighi MR, Żur KK. On the selected problems of time-dependent dynamics of composite truncated conical shells-like aerospace structures. Commun Nonlinear Sci Numer Simulat 2024;130:107717. https://doi.org/10.1016/j.cnsns.2023.107717
39. Gao Z, Shi X, Huang Z, Zhong R, Wang Q. Spectro-geometric solutions for random vibration of functionally graded graphene platelet reinforced conical shells. Thin-Walled Struct 2024;195:111410. https://doi.org/10.1016/j.tws.2023.111410.

40. Li Z, Wang Q, Qin QYB. Stochastic vibration response of multilayer FG-GPLRC truncated conical shell subjected to moving random loads. J Vib Eng Technol 2025;13:179. https://doi.org/10.1007/s42417-024-01715-3.
41. Heydarpour Y, Malekzadeh P, Dimitri R, Tornabene F. Thermoelastic analysis of rotating multilayer FG-GPLRC truncated conical shells based on a coupled TDQM-NURBS scheme. Compos Struct 2020; 235:111707. https://doi.org/10.1016/j.compstruct.2019.111707.
42. Mohammadlou V, Khoddami Maraghi Z, Ghorbanpour Arani A. Thermoelastic analysis of axisymmetric conical shells: Investigating stress–strain response under uniform heat flow with semi-coupled approach. Numer Heat Tr A-Appl 2024; https://doi.org/10.1080/10407782.2024.2326943
43. Heydarpour Y, Malekzadeh P, Zhu H, Mohammadzaheri M. Non-Fourier heat transfer analysis of sandwich conical shells with GPLs reinforced face sheets and porous core under moving heat flux. Results Phys 2025;73:108240. https://doi.org/10.1016/j.rinp.2025.108240.
44. Duc ND, Anh VTT, Cong PH. Nonlinear axisymmetric response of FGM shallow spherical shells on elastic foundations under uniform external pressure and temperature. Eur J Mech A-Solid 2014; 45:80-89. https://doi.org/10.1016/j.euromechsol.2013.11.008.
45. Duc ND. Nonlinear static and dynamic stability of functionally graded plates and shells. Vietnam National University Press, Hanoi, 2014.
46. Chu K, Jia C, Li W. Effective Thermal Conductivity of Graphene-Based Composites. Appl Phys Lett 2012;101: Article ID: 121916. http://dx.doi.org/10.1063/1.4754120.
47. Chu K, Jia C-C, Li W-S. "Erratum: "Effective thermal conductivity of graphene-based composites," Appl Phys Lett 2012;101: 209902–209902-1. DOI: 10.1063/1.4766743.
48. Lord HW, Shulman Y. A generalized dynamical theory of thermoelasticity. J Mech Phys Solids 1967;15:299–309. https://doi.org/10.1016/0022-5096(67)90024-5.
49. Malekzadeh P, Mohebpour SR, Heydarpour Y. Nonlocal effect on the free vibration of short nanotubes embedded in an elastic medium. Acta Mech 2012;223:1341-1350. https://doi.org/10.1007/s00707-012-0621-4.
50. Heydarpour Y, Aghdam MM. A coupled integral–differential quadrature and B-spline-based multi-step technique for transient analysis of VSCL plates. Acta Mech 2017;228:2965–2986. https://doi.org/10.1007/s00707-017-1850-3.

51. Heydarpour Y, Aghdam MM. Response of VSCL plates under moving load using a mixed integral-differential quadrature and novel NURBS based multi-step method. Compos B Eng 2018;140:260-280. https://doi.org/10.1016/j.compositesb.2017.07.066.
52. Heydarpour Y, Malekzadeh P. Dynamic stability of cylindrical nanoshells under combined static and periodic axial loads. J Braz Soc Mech Sci Eng 2019;41:184. https://doi.org/10.1007/s40430-019-1675-1.
53. Heydarpour Y, Malekzadeh P, Żur KK. Explosive blast loading effect on transient mechanical responses of aircraft panels with curvilinear fibers: 3D elasticity approach. Compos Struct 2024;334:117967. https://doi.org/10.1016/j.compstruct.2024.117967.
54. Heydarpour Y, Aghdam MM. A new multistep technique based on the nonuniform rational basis spline curves for nonlinear transient heat transfer analysis of functionally graded truncated cone. Heat Transfer Eng 2019;40:588-603. https://doi.org/10.1080/01457632.2018.1436422.
55. Heydarpour Y, Malekzadeh P. Thermoelastic Analysis of Multilayered FG Spherical Shells Based on Lord–Shulman Theory. Iran J Sci Technol Trans Mech Eng 2019;43:845–867. https://doi.org/10.1007/s40997-018-0199-0.
56. Heydarpour Y, Mohammadzaheri M, Ghodsi M, Soltani P, Al-Jahwari F, Bahadur I, Al-Amri B. A coupled DQ-Heaviside-NURBS approach to investigate nonlinear dynamic response of GRE cylindrical shells under impulse loads. Thin-Walled Struct 2021;165:107958. https://doi.org/10.1016/j.tws.2021.107958.
57. Heydarpour Y, Malekzadeh P. Three-dimensional non-Fourier heat transfer analysis of multilayer functionally graded graphene platelets reinforced composite truncated conical shells. Heat Transfer Eng 2021;42(15):1303-1318. https://doi.org/10.1080/01457632.2020.1785700.
58. Heydarpour Y, Malekzadeh P, Zhu H. Three-Dimensional Response of Multilayer FG-GPLRC Spherical Panels Under Blast Loading. Int J Struct Stab Dy 2022;22(11):2250111. https://doi.org/10.1142/S0219455422501115.
59. Peng XL, Li XF. Thermal stress in rotating functionally graded hollow circular disks. Compos Struct 2010; 92:1896–1904. https://doi.org/10.1016/j.compstruct.2010.01.008.
60. Santos H, Mota Soares CM, Mota Soares CA, Reddy JN. A semi-analytical finite element model for the analysis of cylindrical shells made of functionally graded materials under

thermal shock. Compos Struct 2008;86:10-21. https://doi.org/10.1016/j.compstruct.2008.03.004.

61. Bhangale RK, Ganesan K, Padmanabhan C. Linear thermoelastic buckling and free vibration behaviour of functionally graded truncated conical shells. J Sound Vib 2006;292:341-371. https://doi.org/10.1016/j.jsv.2005.07.039.

Table 1. Material properties of the epoxy and GPLs [41].

Material	Epoxy	GPLs
E (GPa)	3	1010
ν	0.34	0.186
$\rho\left(\mathrm{kg/m^3}\right)$	1200	1062.5
c (J/kgK)	1110	644
$\alpha\left(1/\mathrm{K}\right)$	60×10^{-6}	5×10^{-6}
k (W/mK)	0.246	3000

Table 2. Comparison between the convergence and CPU time requirement of the NURBS-based multi-step technique and the Newmark's scheme for the analysis of the clamped multilayer truncated conical shell with the GPLRC-FS and GPLRC-PC $\left[W_{GPL}=1\%,\ \zeta=0,\eta=0.5,\ e_0=0.4,\ \text{porosity type 1},\ \beta=15^{\circ},\ F_{\mathrm{o}}=1,\ u^{*}=0.1\left(\mathrm{cm/s}\right),\ \tau=0.01\right]$.

	NURBS-based scheme			Newmark's scheme		
N_t	T^{*}	U	CPU time (s)	T^{*}	U	CPU time (s)
25	18.5398	0.9742	0.023179	18.5498	0.9570	14.022937
50	18.5620	0.9833	0.039076	18.5517	0.9862	29.594114
100	18.5696	0.9975	0.054275	18.5543	0.9988	54.511361
200	18.5743	1.0031	0.079816	18.5866	1.0043	107.38951
300	18.5779	1.0058	0.185271	18.5954	1.0061	162.56988
400	18.5803	1.0062	0.225409	18.5967	1.0065	210.23766
500	18.5816	1.0062	0.278912	18.5981	1.0066	304.07169

Table 3. Comparison of the results for the freely rotating FG annular disk subjected to non-uniform temperature rise $\left[R_i / R_o = 0.2,\ L / R_o = 0.05,\ R_o = 1\,\mathrm{m},\ \Omega = 600\left(\mathrm{Rad/s}\right),\ \eta = 0.5\right]$.

		Present			Analytical [59]		
n	ς	U	$\Sigma_{\theta\theta}$	Σ_{rr}	U	$\Sigma_{\theta\theta}$	Σ_{rr}
0.5	0	0.1813	0.3691	1.41E-4	0.1813	0.3689	0
	0.5	0.2546	0.1730	0.1290	0.2547	0.1735	0.1294
	1	0.4054	0.0101	-1.24E-4	0.4054	0.0102	0
0	0	0.1470	0.6675	-1.51E-4	0.1468	0.6680	0
	0.5	0.2381	0.1639	0.1583	0.2381	0.1636	0.1580
	1	0.3997	0.005	-3.62E-4	0.3994	4.73E-3	0
-0.5	0	0.1197	1.2163	-4.60E-4	0.1194	1.2152	0
	0.5	0.2267	0.1464	0.1891	0.2267	0.1465	0.1893
	1	0.3965	0.0021	-1.43E-5	0.3961	1.74E-3	0

Table 4. Material properties of ceramic (Zirconia) and metal (steel) [60].

Material	Zirconia	steel
$k\left(\mathrm{W/cm^0C}\right)$	2.09	20
$\rho\left(\mathrm{kg/m^3}\right)$	5700	8166
$C_v\left(\mathrm{J/kg^\circ C}\right)$	531.9	325.35
$E\left(\mathrm{MPa}\right)$	168.06	207.79
$\alpha\left(\mathrm{1/^\circ C}\right)$	2.3×10^{-4}	1.5×10^{-5}
ν	0.298	0.3178

Table 5. The influences of the load velocity and porosity amount on the results for the clamped multilayer truncated conical shell with the GPLRC-FS and GPLRC-PC $\left[W_{GPL} = 0.3\%,\ \zeta = \eta = 0.5,\ \text{porosity type } 1,\ \beta = 15^\circ,\ \tau = 0.03\right]$

		$Fo = 0.5$			$Fo = 1$		
e_0	u^*(cm/s)	T^*	U	Σ_{zz}	T^*	U	Σ_{zz}
0	0.01	143.6198	25.1383	-0.0802	66.4413	7.1292	-0.1531
	0.1	13.8985	20.4797	0.0298	17.4160	1.9781	-0.0372
	1	0.1812	19.8943	0.0493	0.4331	0.2636	-0.0012
0.	0.01	83.5917	27.3651	-0.1162	68.3034	7.3584	-0.1594
	0.1	16.4484	22.4693	0.0024	19.5281	2.1887	-0.0419
	1	0.3768	21.7591	0.0274	1.1982	0.2942	-0.0032
0.	0.01	87.4499	29.2158	-0.1664	69.6473	7.6196	-0.1637
	0.1	17.9356	24.0962	-0.0414	20.7403	2.3379	-0.0445
	1	0.2104	23.2775	-0.0107	1.9920	0.3168	-0.0051

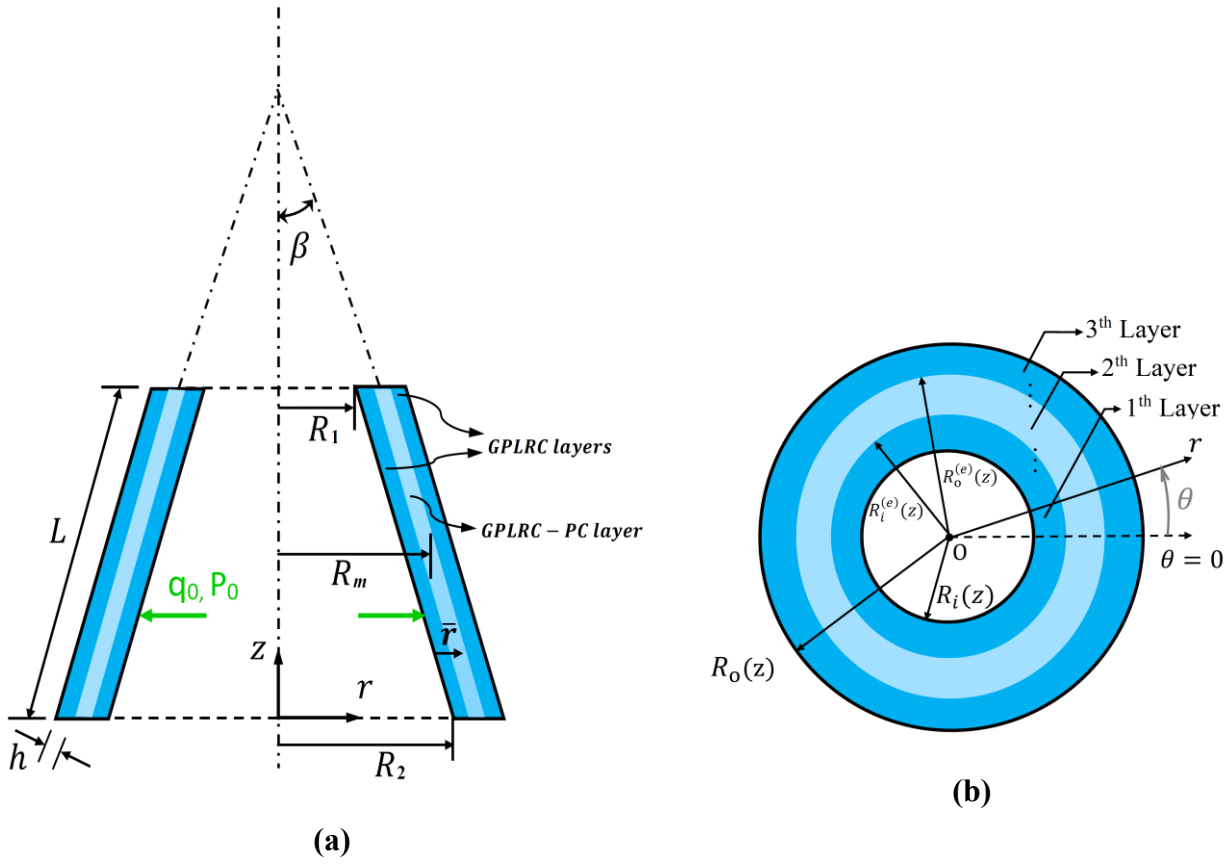

Fig. 1: The geometry and coordinate system of multilayer GPLRC truncated conical shell.

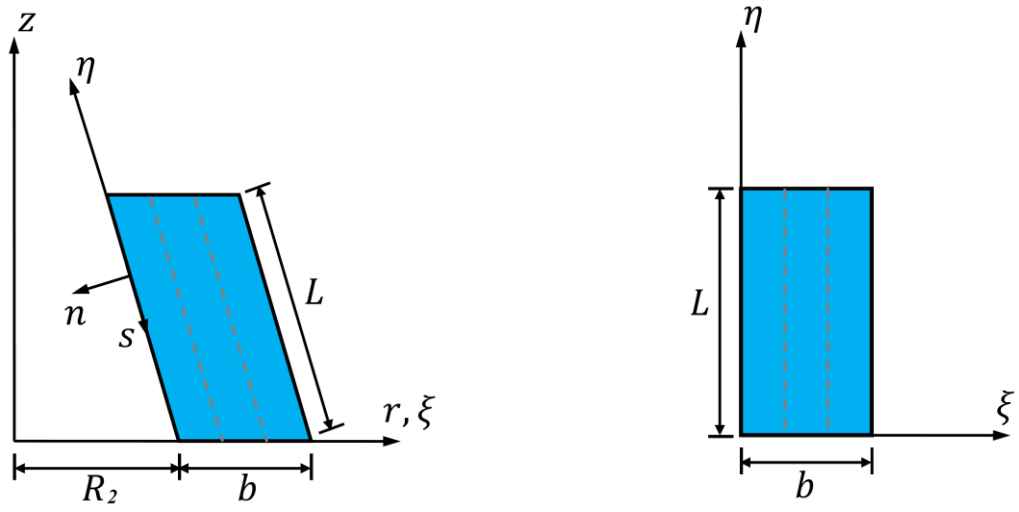

(a) The physical domain

(b) The computational domain

Fig. 2 The physical and computational domains.

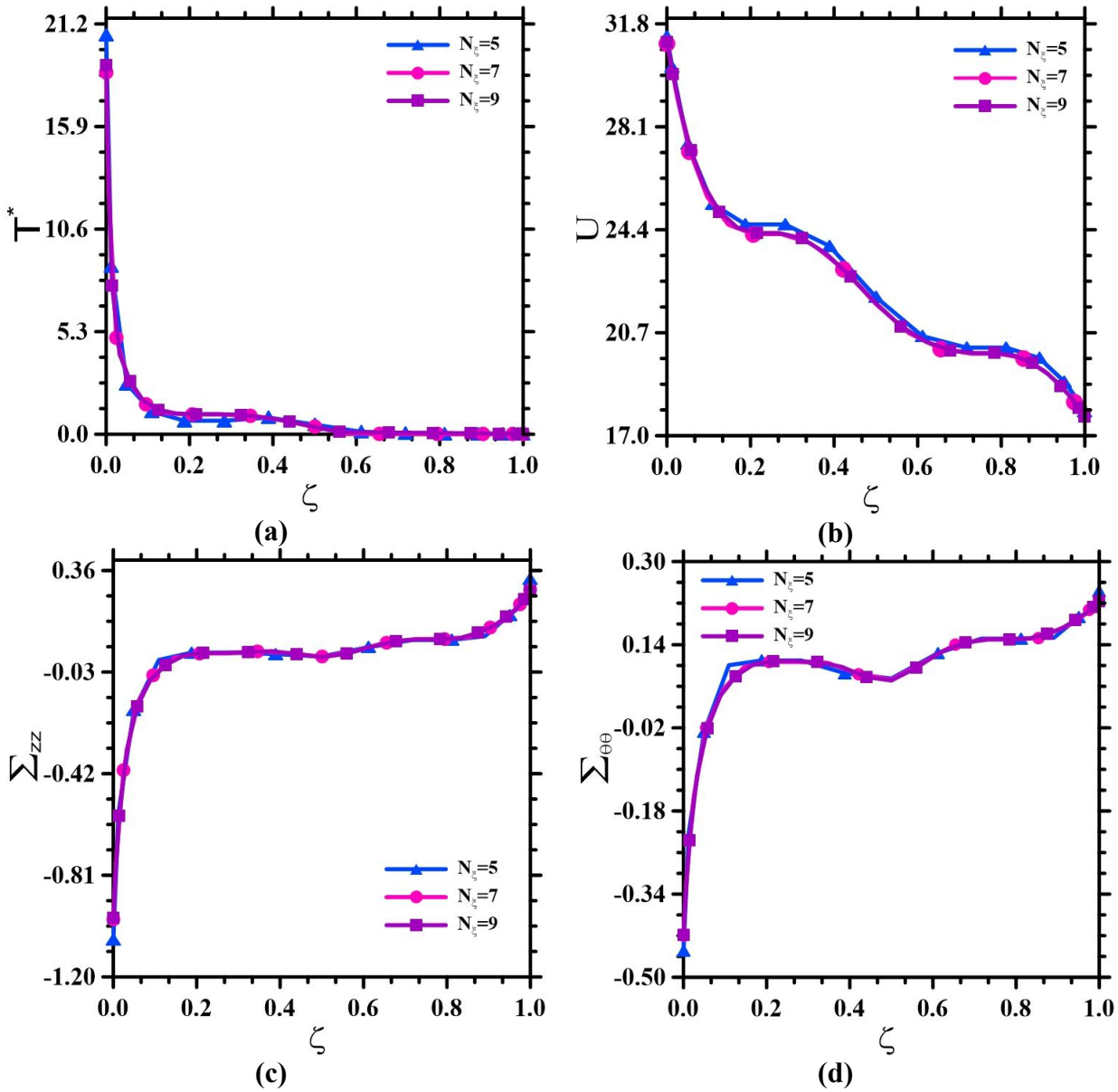

Fig. 3: Through-the-thickness variation of the results for the clamped multilayer truncated conical shell with the GPLRC-FS and GPLRC-PC, and different DQ number of grid point along the radial direction $\left[W_{GPL}=0.3\%,\ \eta=0.5,\ e_0=0.4,\ \text{porosity type 1},\ \beta=15^{\circ},\ N_\eta=29,\ Fo=0.5,\ u^*=1(\text{cm/s}),\ \tau=0.03\right]$.

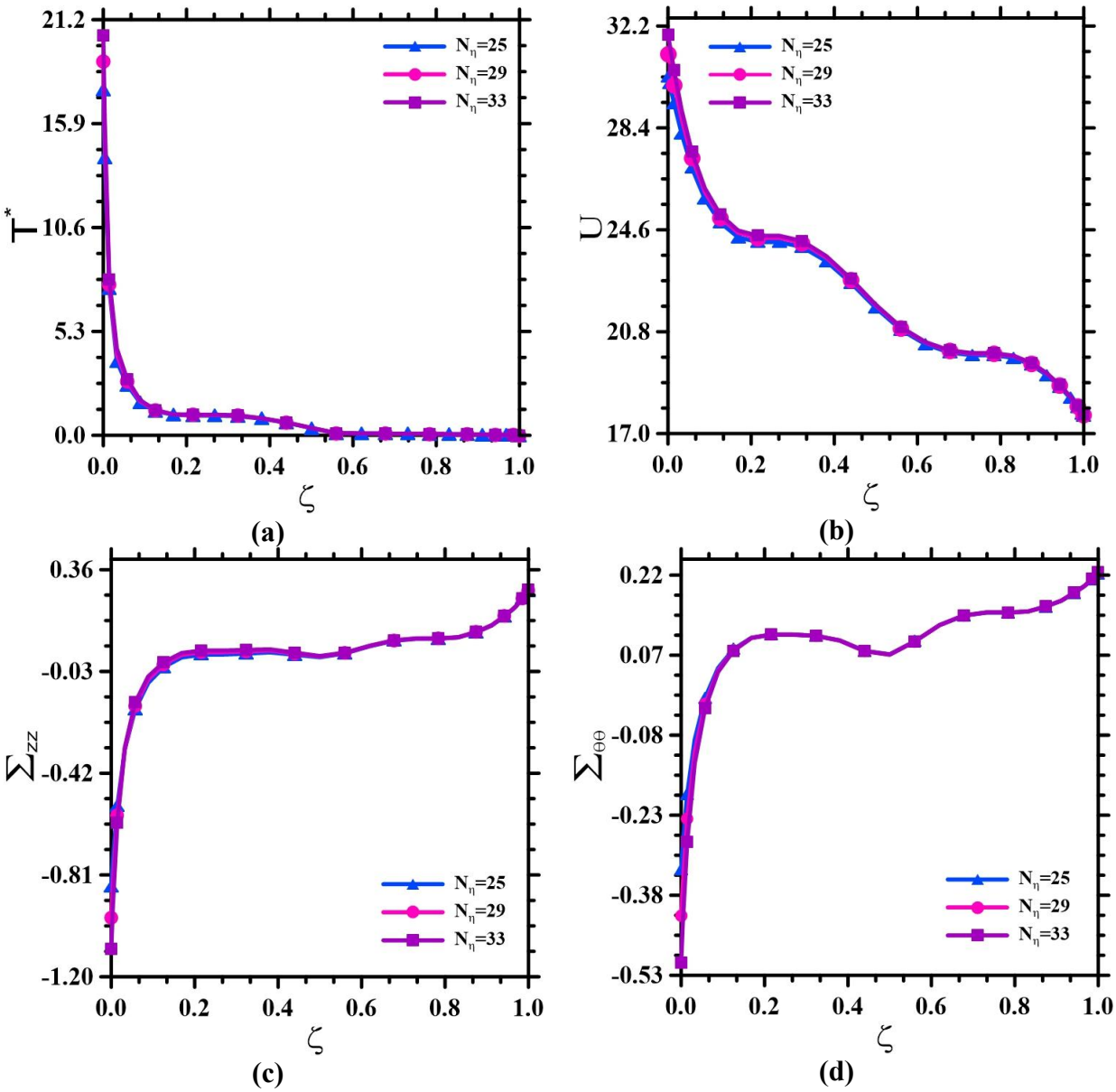

Fig. 4: Through-the-thickness variations of the results for the clamped multilayer truncated conical shell with the GPLRC-FS and GPLRC-PC, and different DQ number of grid point along the axial direction $\left[W_{GPL}=0.3\%,\ \eta=0.5,\ e_0=0.4,\ \text{porosity type 1},\ \beta=15^{\circ},\ N_{\xi}=9,\ Fo=0.5,\ u^{*}=1(\text{cm/s}),\ \tau=0.03\right]$.

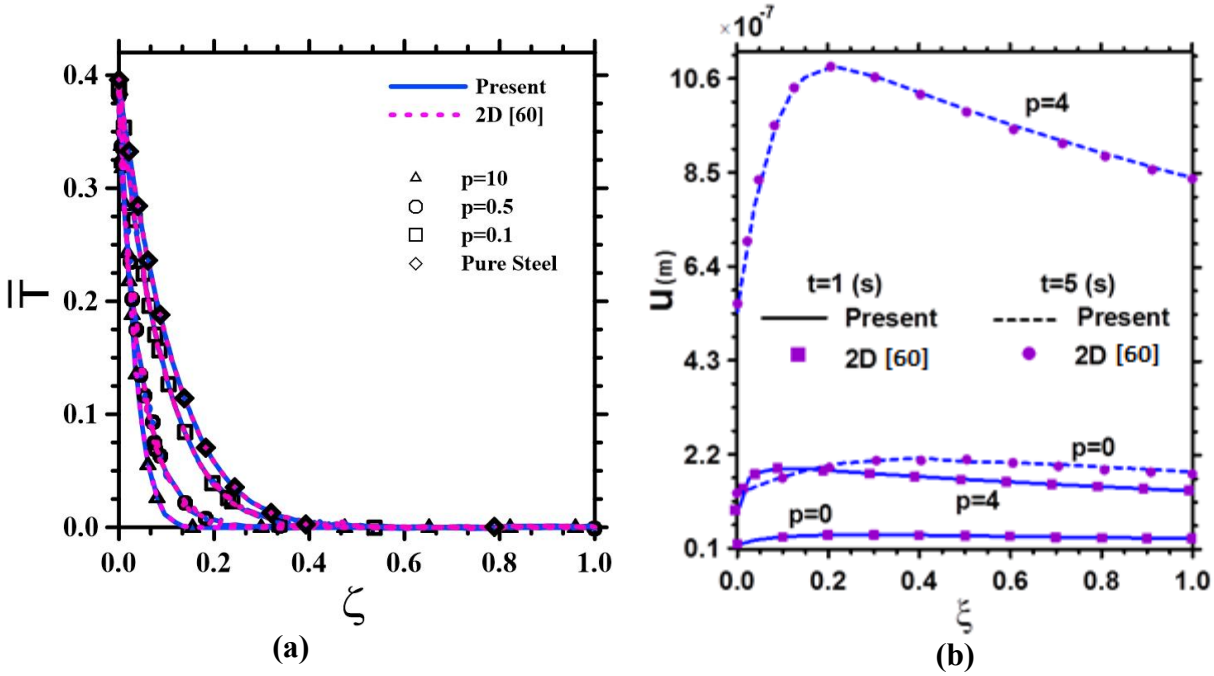

Fig. 5: Transient non-dimensional temperature distribution and radial displacement across the thickness for a FG hollow cylinder subjected to a prescribed temperature on its inner surface $\left[R_{\mathrm{i}}=4\left(\mathrm{cm}\right),\ R_{\mathrm{o}}=6\left(\mathrm{cm}\right),\ t\text{=}1\left(\mathrm{s}\right),\ L=20\left(\mathrm{cm}\right),\ \overline{T}=T/T_{0}\ ,\ \eta=0.5\right]$.

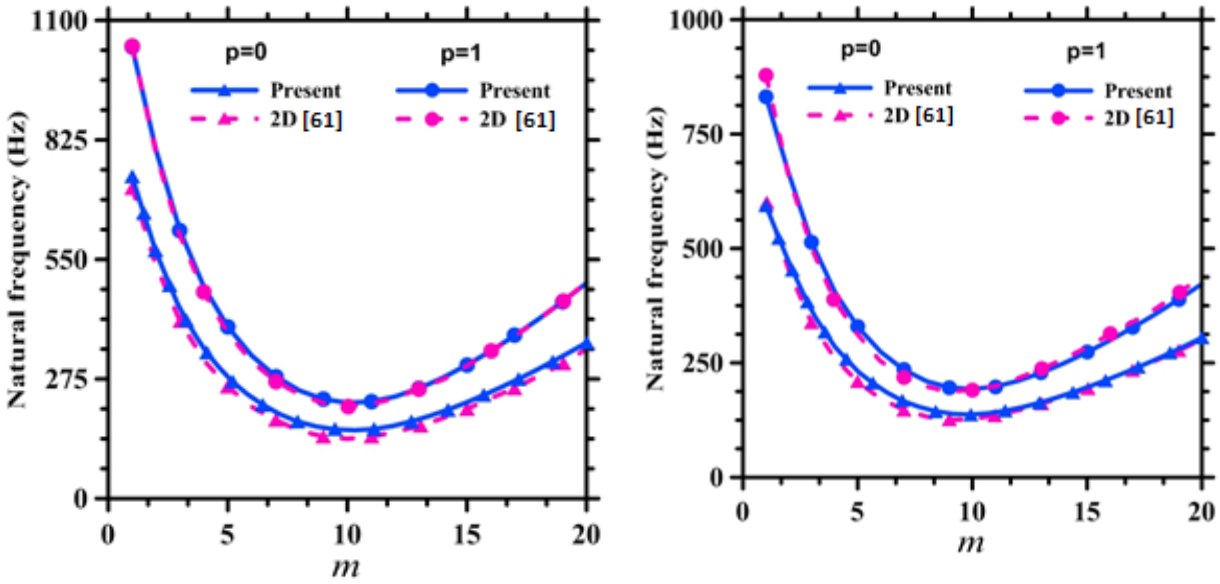

Fig. 6: First natural frequency corresponding to the first twelve circumferential wave numbers of the clamped FG truncated conical shell $\left(\overline{R}/H=292,\ L/\overline{R}=1.0438,\ \overline{R}=\dfrac{R_{1}+R_{2}}{2}\right)$.

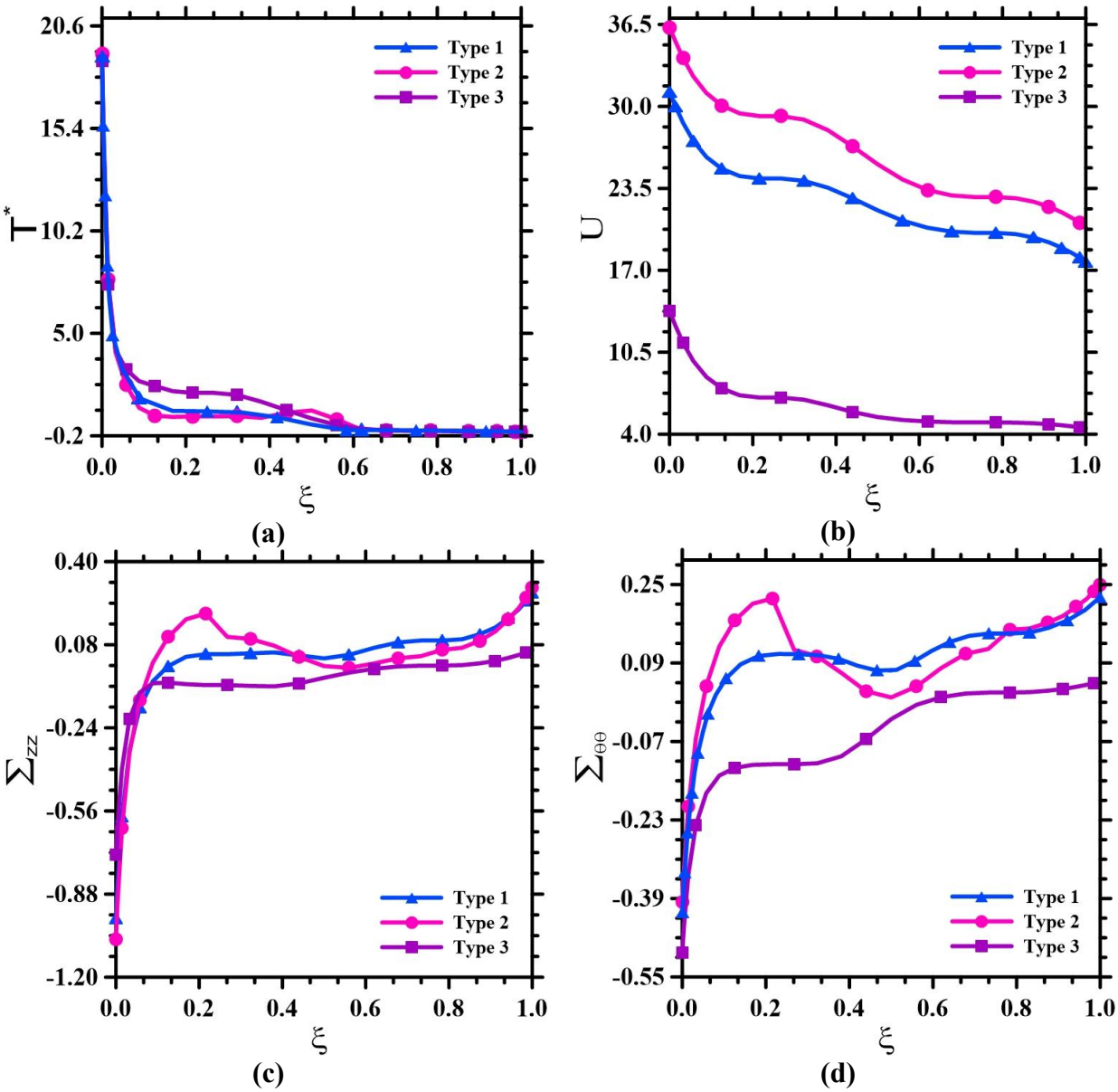

Fig. 7: Effects of porosity distribution pattern on the through-the-thickness variation of the results of the clamped multilayer truncated conical shell with the GPLRC-FS and GPLRC-PC $\left[W_{GPL}=0.3\%,\ \eta=0.5,\ Fo=0.5,\ e_0=0.4,\ \beta=15^{\circ},\ u^*=1(\text{cm/s}),\ \tau=0.03\right]$.

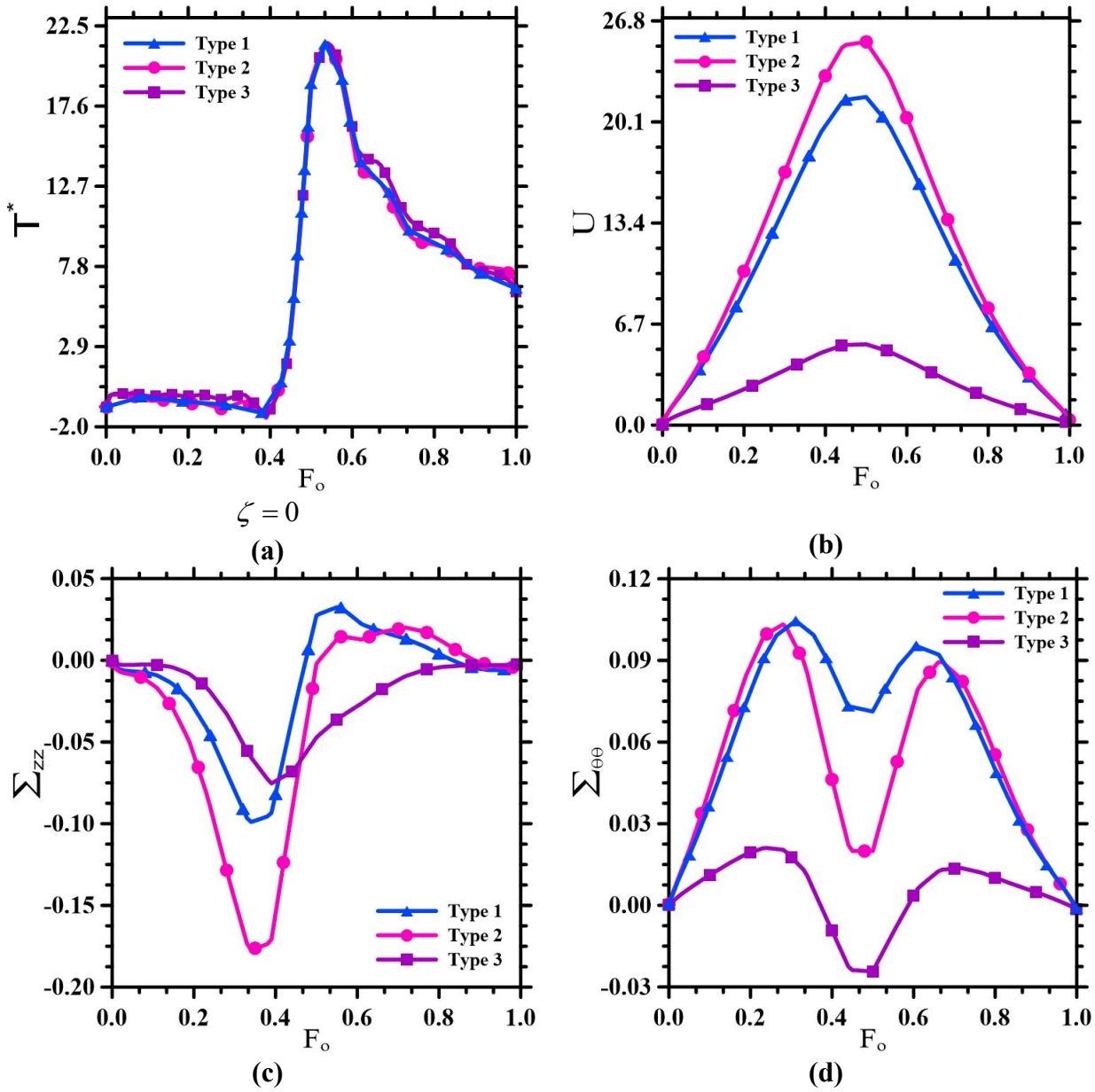

Fig. 8: Effects of porosity distribution pattern on the time histories of the results of the clamped multilayer truncated conical shell with the GPLRC-FS and GPLRC-PC $\left[W_{GPL}=0.3\%,\ \zeta=0.5, \eta=0.5,\ e_0=0.4,\ \beta=15^{\circ},\ u^{*}=1(\text{cm/s}),\ \tau=0.03\right]$.

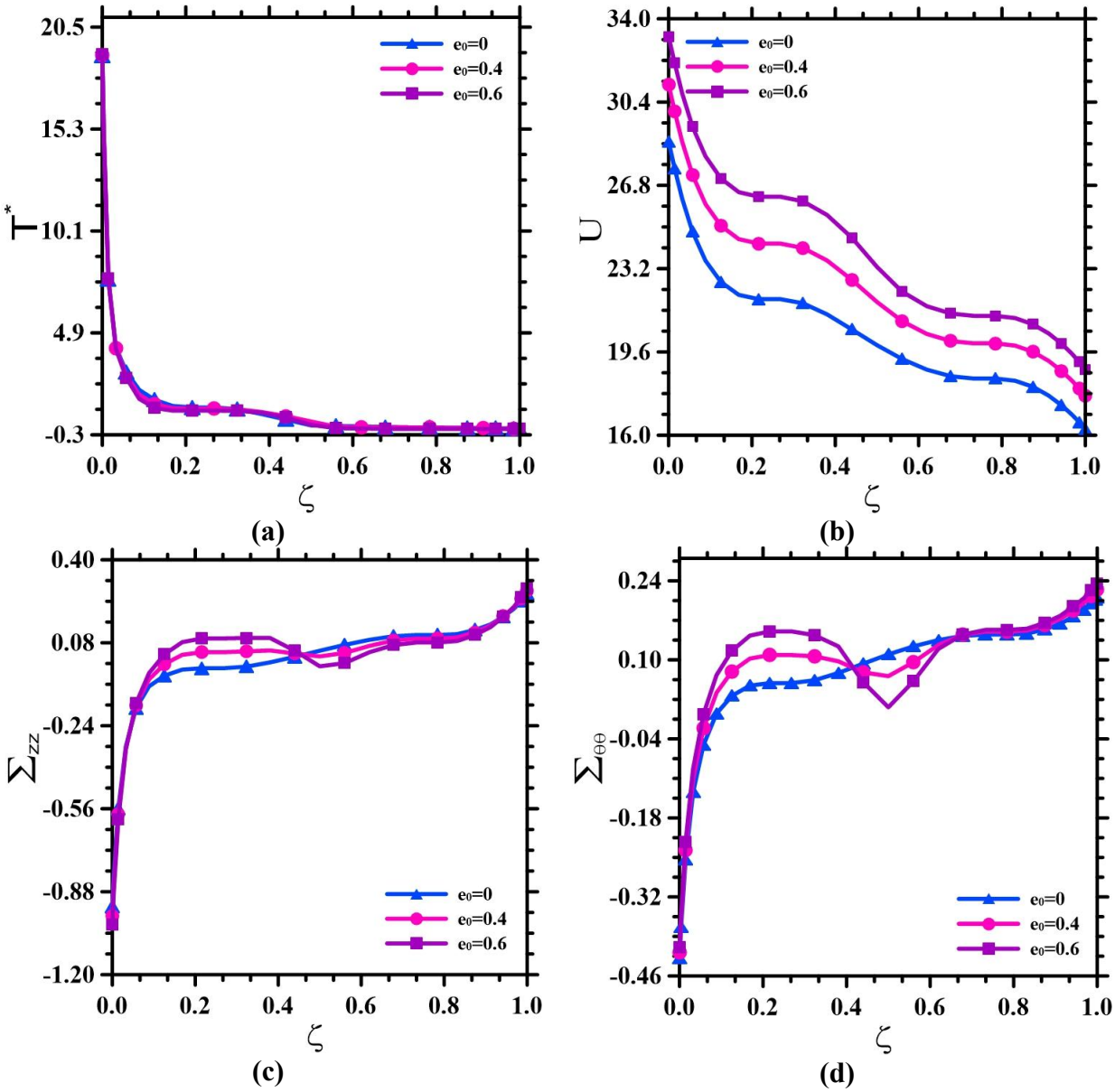

Fig. 9: Effects of porosity amounts on the through-the-thickness variation of the results of the clamped multilayer truncated conical shell with the GPLRC-FS and GPLRC-PC $\left[W_{GPL}=0.3\%,\right.$ $\eta=0.5,\ Fo=0.5,$ porosity type 1, $\beta=15^{\circ}$, $u^{*}=1(\mathrm{cm/s}),\ \tau=0.03\left.\right]$.

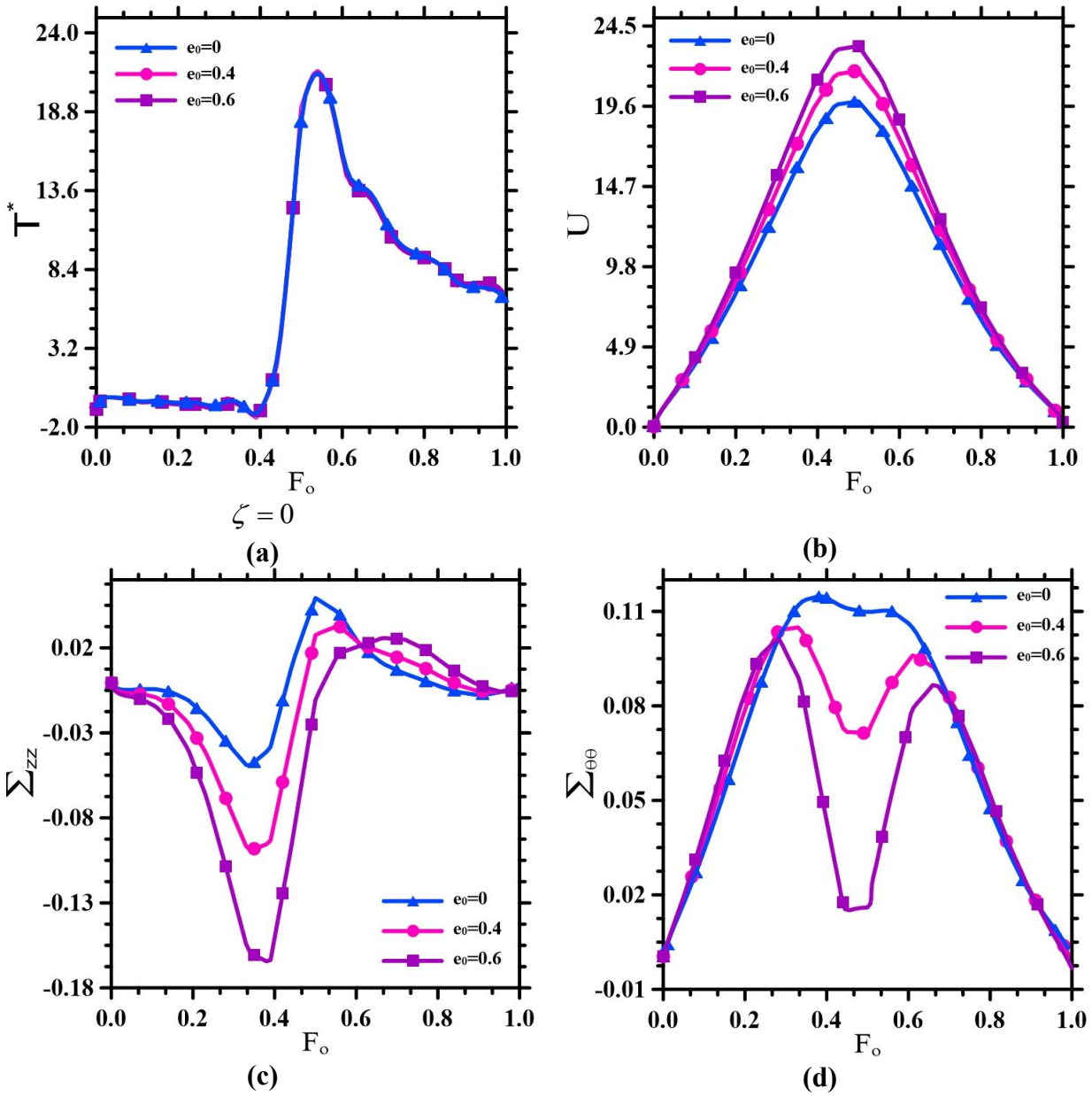

Fig. 10: Effects of porosity amounts on the time histories of the results of the clamped multilayer truncated conical shell with the GPLRC-FS and GPLRC-PC $\left[W_{GPL}=0.3\%,\ \zeta=0.5,\eta=0.5,\right.$ porosity type 1, $\beta=15^{\circ}$, $u^{*}=1(\mathrm{cm/s}),\ \tau=0.03\left.\right]$.

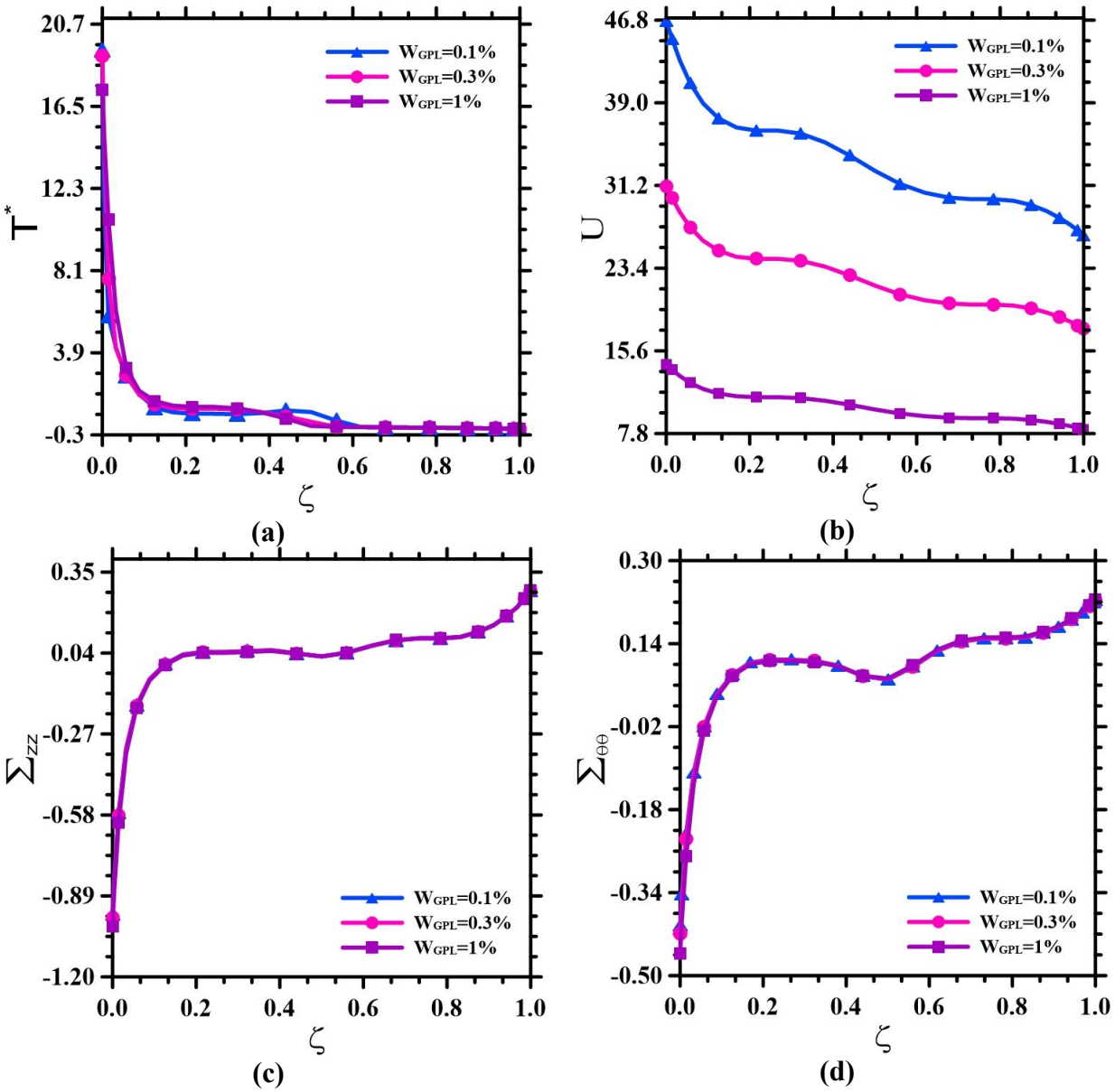

Fig. 11: Effects of GPLs weight fraction on the through-the-thickness variation of the results of the clamped multilayer truncated conical shell with the GPLRC-FS and GPLRC-PC $[\eta = 0.5,$ $Fo = 0.5,\ e_0 = 0.4,$ porosity type 1, $\beta = 15^{\circ},\ u^* = 1(\text{cm/s}),\ \tau = 0.03]$.

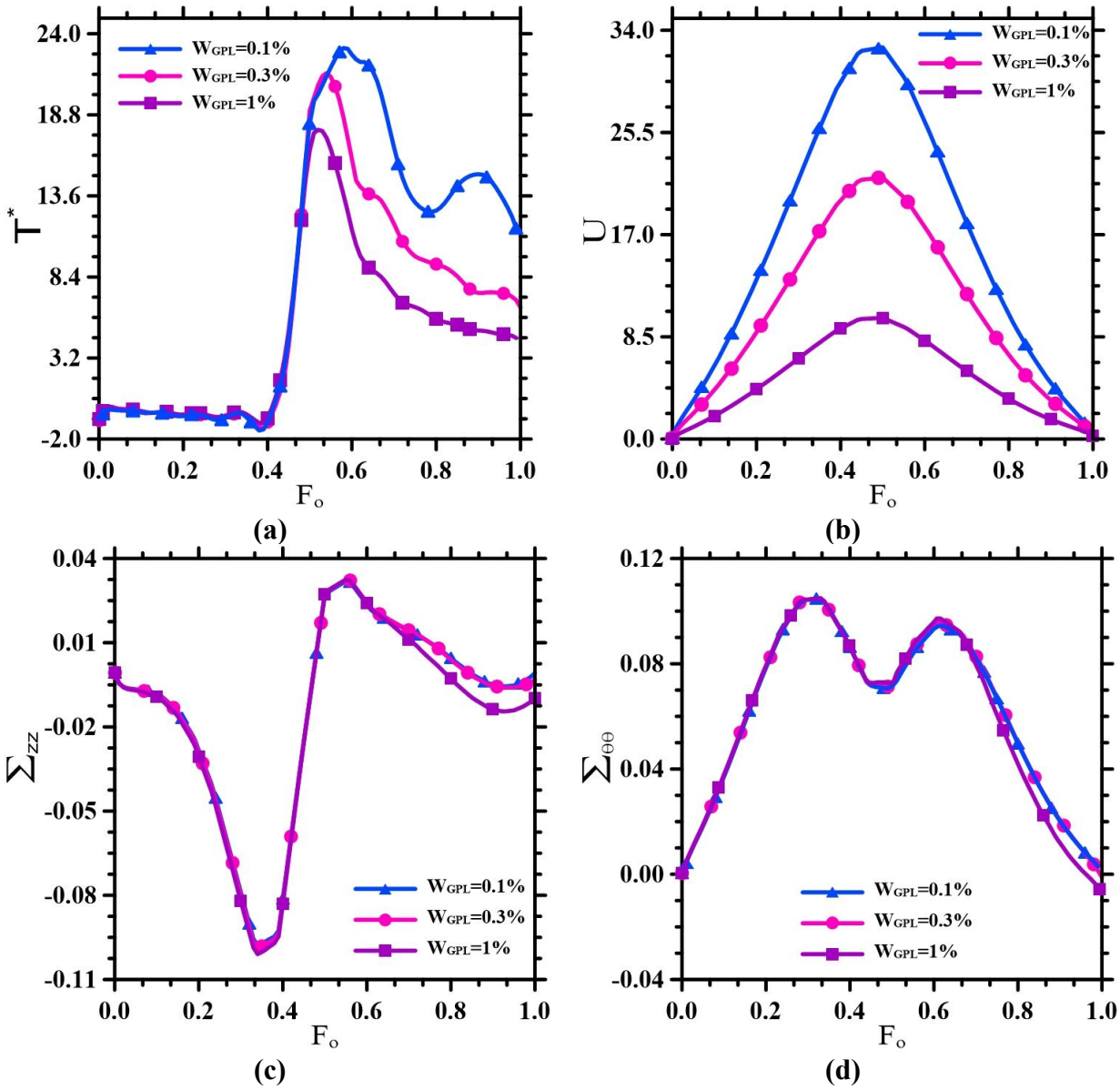

Fig. 12: Effects of GPLs weight fraction on the time histories of the results of the clamped multilayer truncated conical shell with the GPLRC-FS and GPLRC-PC $[\zeta = 0.5, \eta = 0.5, e_0 = 0.4,$ porosity type 1, $\beta = 15^{\circ}$, $u^* = 1(\text{cm/s}), \tau = 0.03]$.

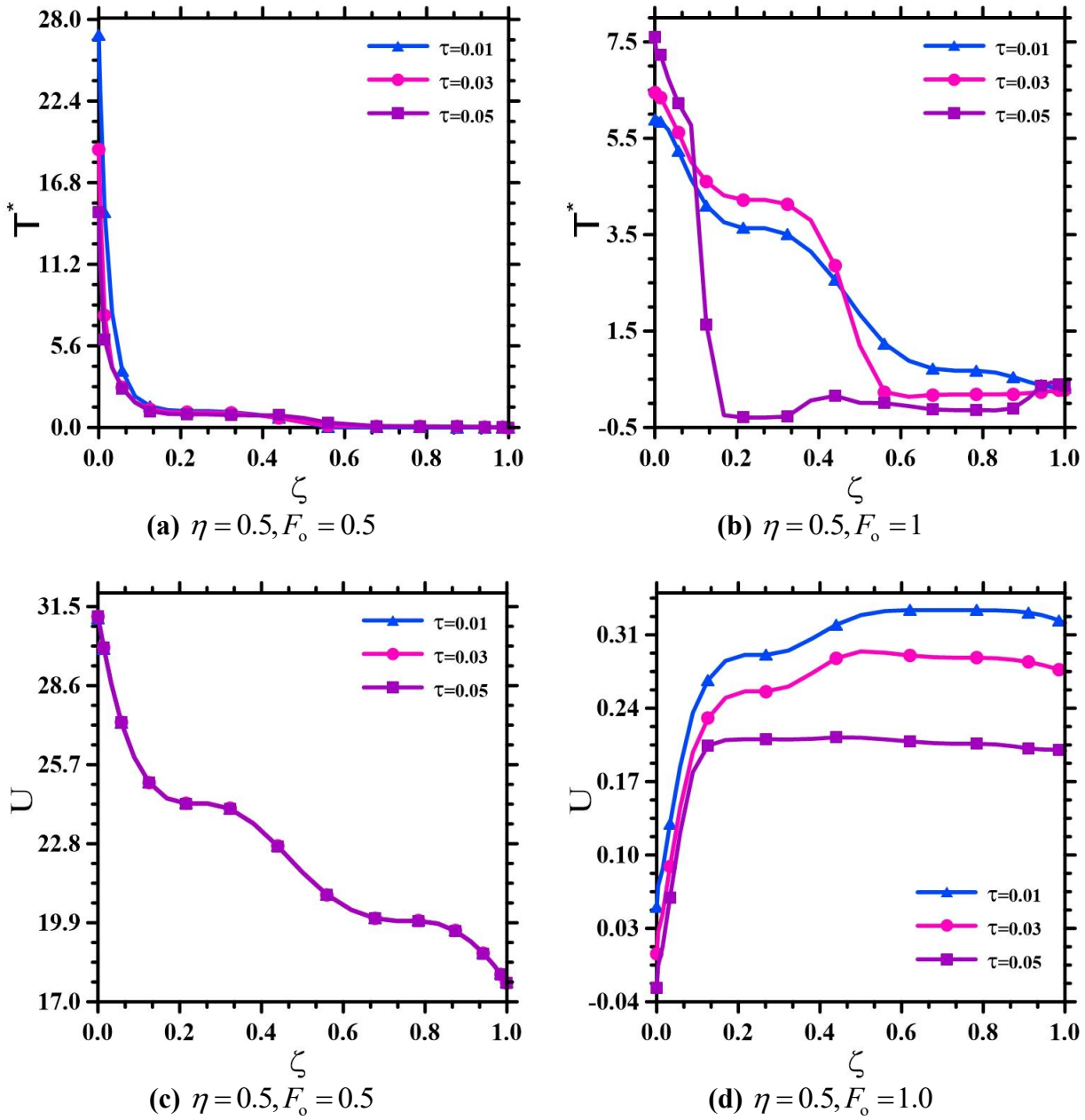

Fig. 13: Effects of the relaxation time on the through-the-thickness variations of the non-dimensional temperature and radial displacement for clamped multilayer truncated conical shell with the GPLRC-FS and GPLRC-PC $\left[W_{GPL}=0.3\%, e_0=0.4,\right.$ porosity type 1, $\beta=15^{\circ}$, $\left.u^{*}=1(\mathrm{cm/s})\right]$.

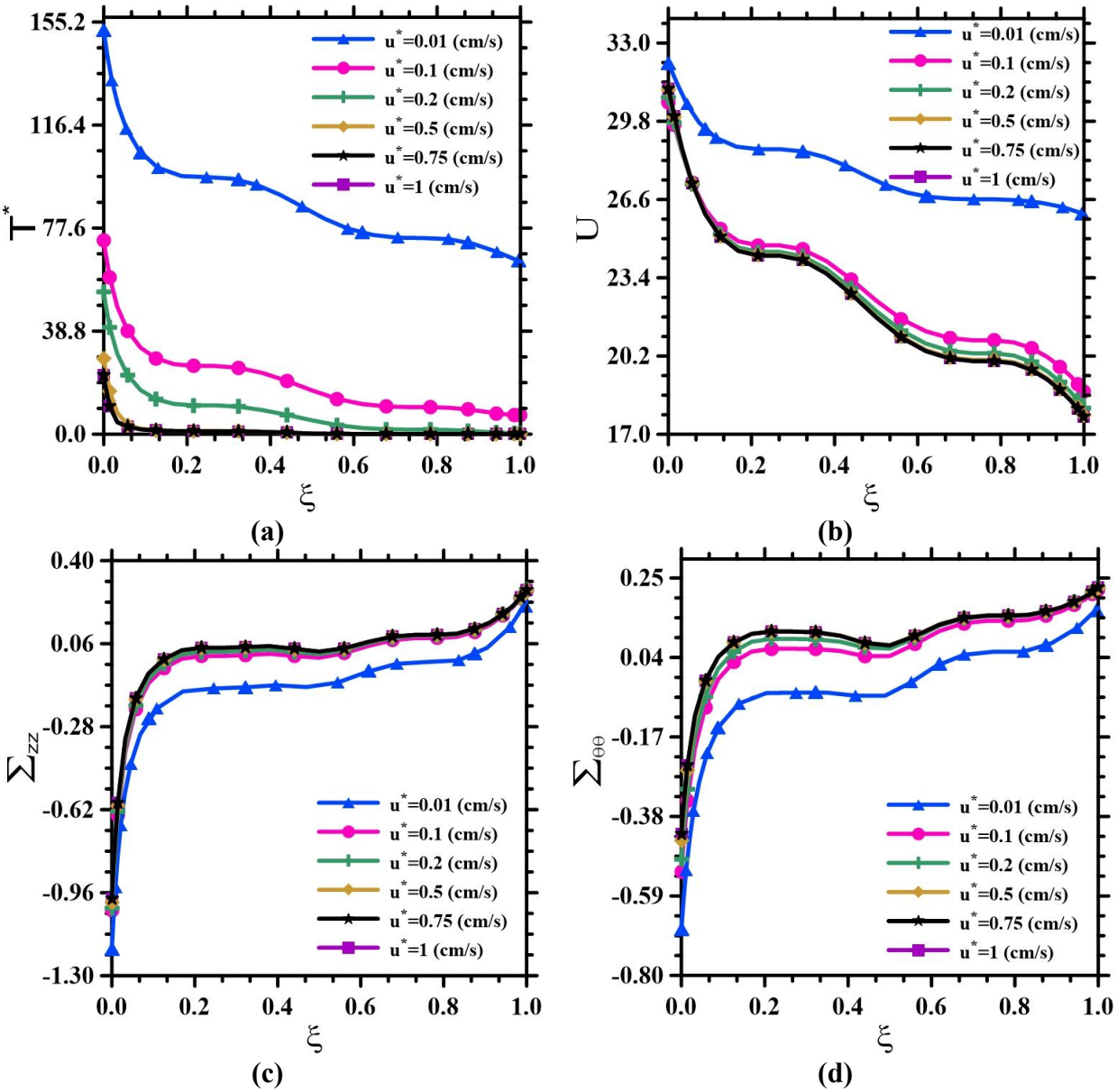

Fig. 14: Effects of speed of the moving heat flux and pressure on the through-the-thickness variation of the results of the clamped multilayer truncated conical shell with the GPLRC-FS and GPLRC-PC $\left[W_{GPL}=0.3\%,\ \eta=0.5,\ Fo=0.5,\ e_0=0.4,\text{porosity type 1},\ \beta=15^{\circ},\ \tau=0.03\right]$.

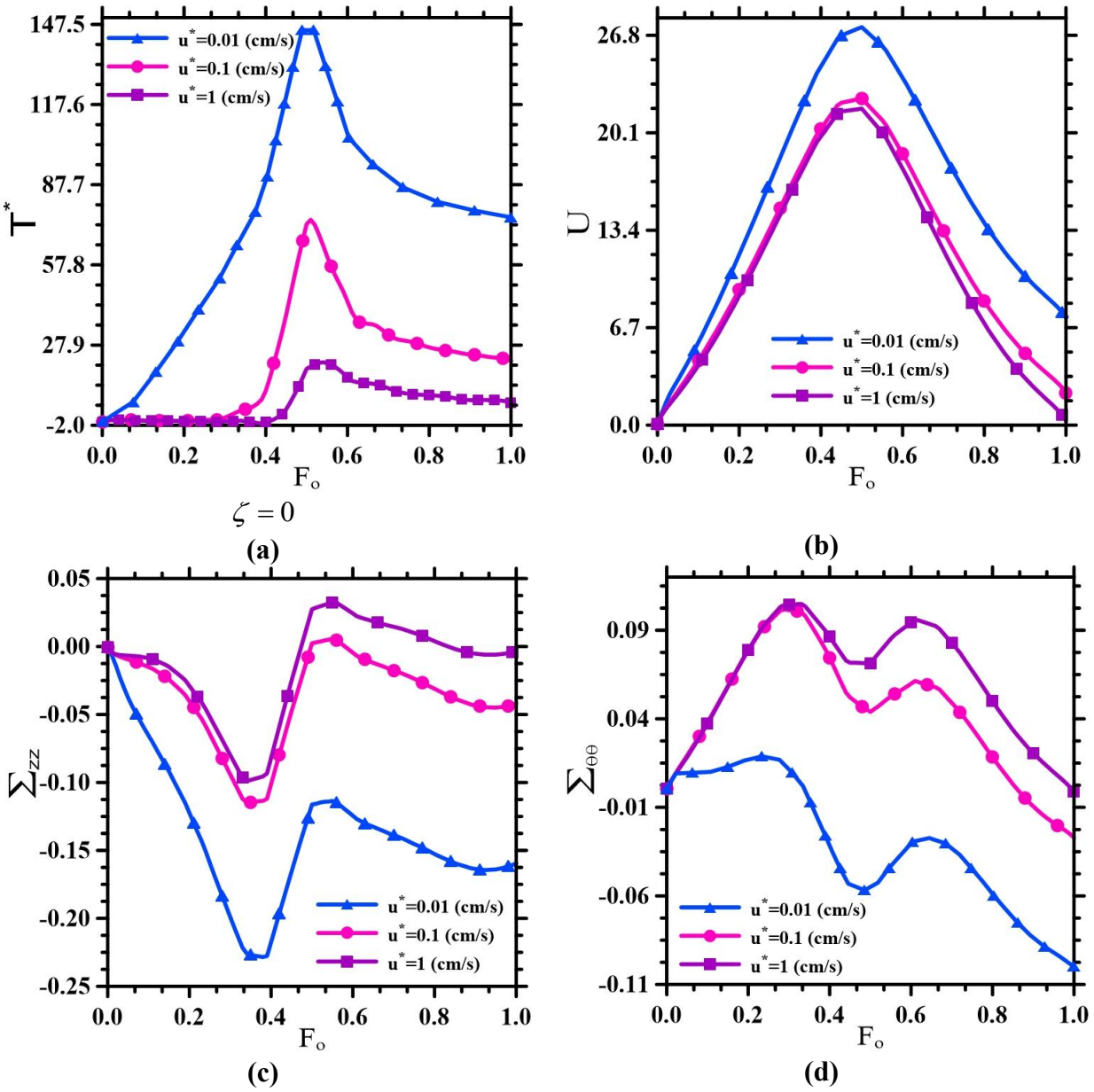

Fig. 15: Effects of speed of the moving heat flux and pressure on the time histories of the results of the clamped multilayer truncated conical shell with the GPLRC-FS and GPLRC-PC $\left[W_{GPL} = 0.3\%,\ \zeta = 0.5, \eta = 0.5,\ e_0 = 0.4,\ \text{porosity type 1}, \beta = 15^{\circ},\ \tau = 0.03\right]$.

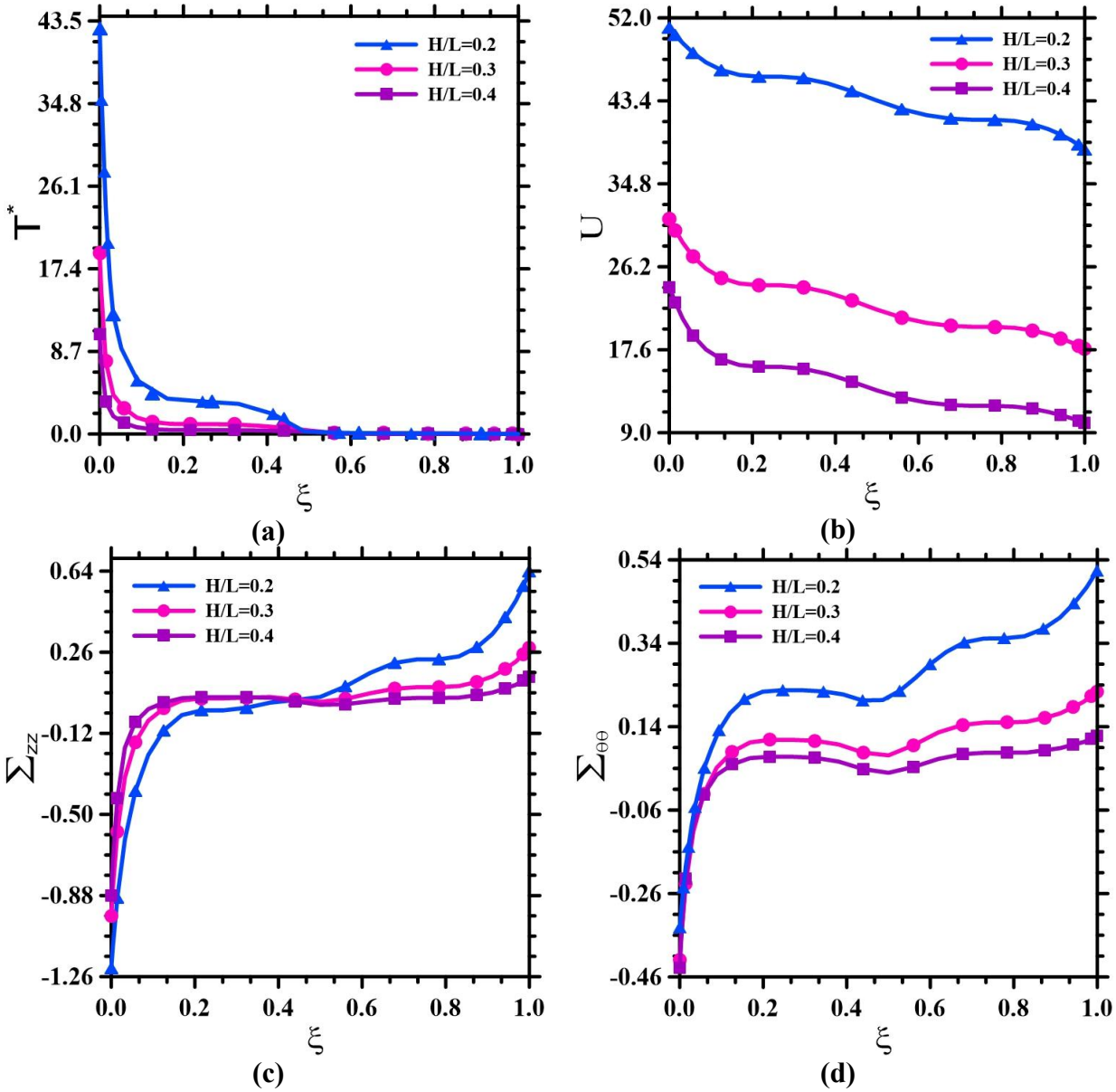

Fig. 16: Effects of the thickness-to-length ratio on the through-the-thickness variation of the results of the clamped multilayer truncated conical shell with the GPLRC-FS and GPLRC-PC $\left[W_{GPL}=0.3\%,\ \eta=0.5,\ Fo=0.5,\ e_0=0.4,\text{porosity type 1},\beta=15^{\circ},\ u^{*}=1(\text{cm/s}),\ \tau=0.03\right]$.

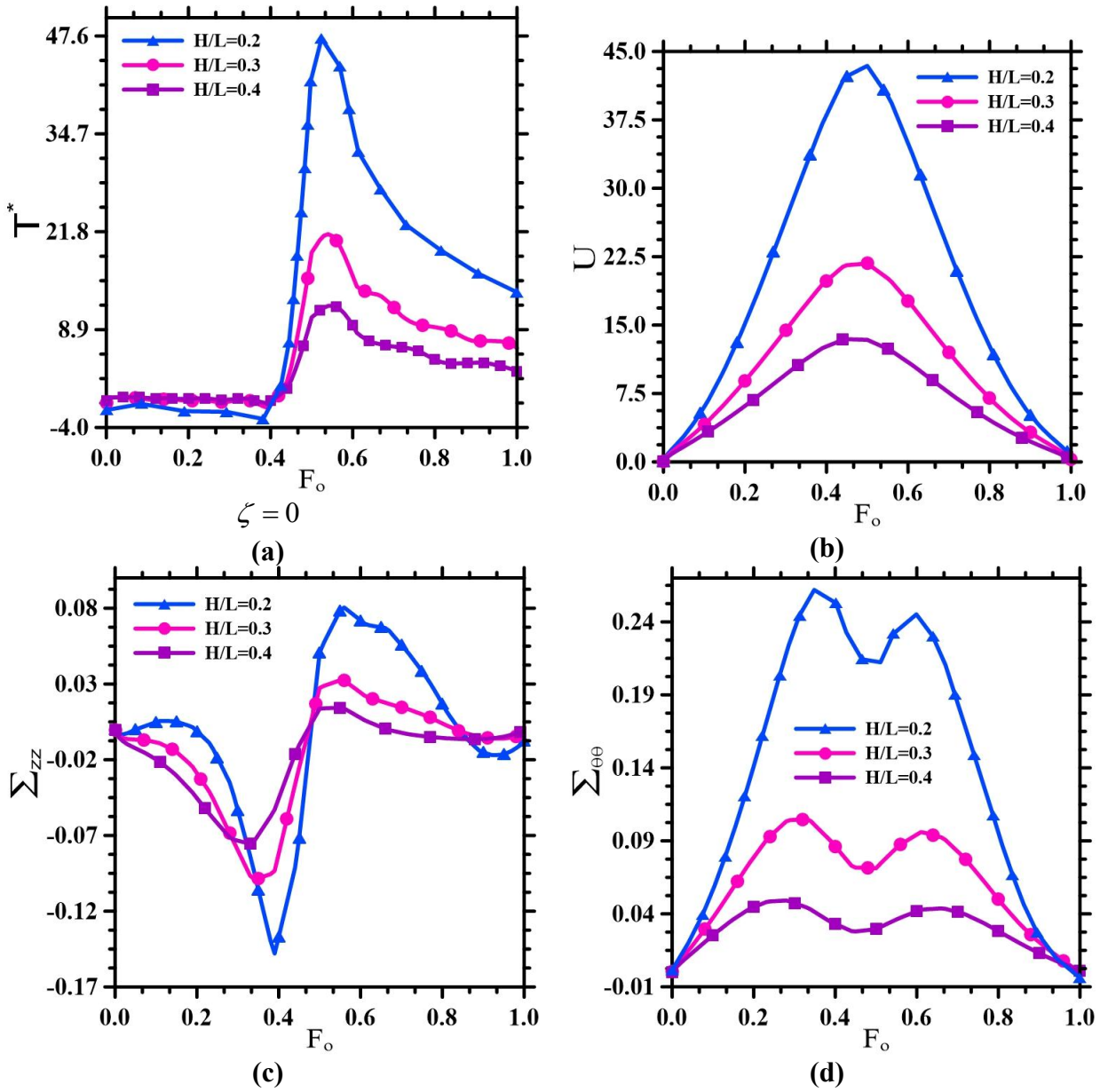

Fig. 17: Effects of the thickness-to-length ratio on the time histories of the results of the clamped multilayer truncated conical shell with the GPLRC-FS and GPLRC-PC $\left[W_{GPL}=0.3\%,\right.$ $\left.\zeta=0.5, \eta=0.5,\ e_0=0.4,\ \text{porosity type 1}, \beta=15^{\circ},\ u^*=1(\text{cm/s}),\ \tau=0.03\right]$.

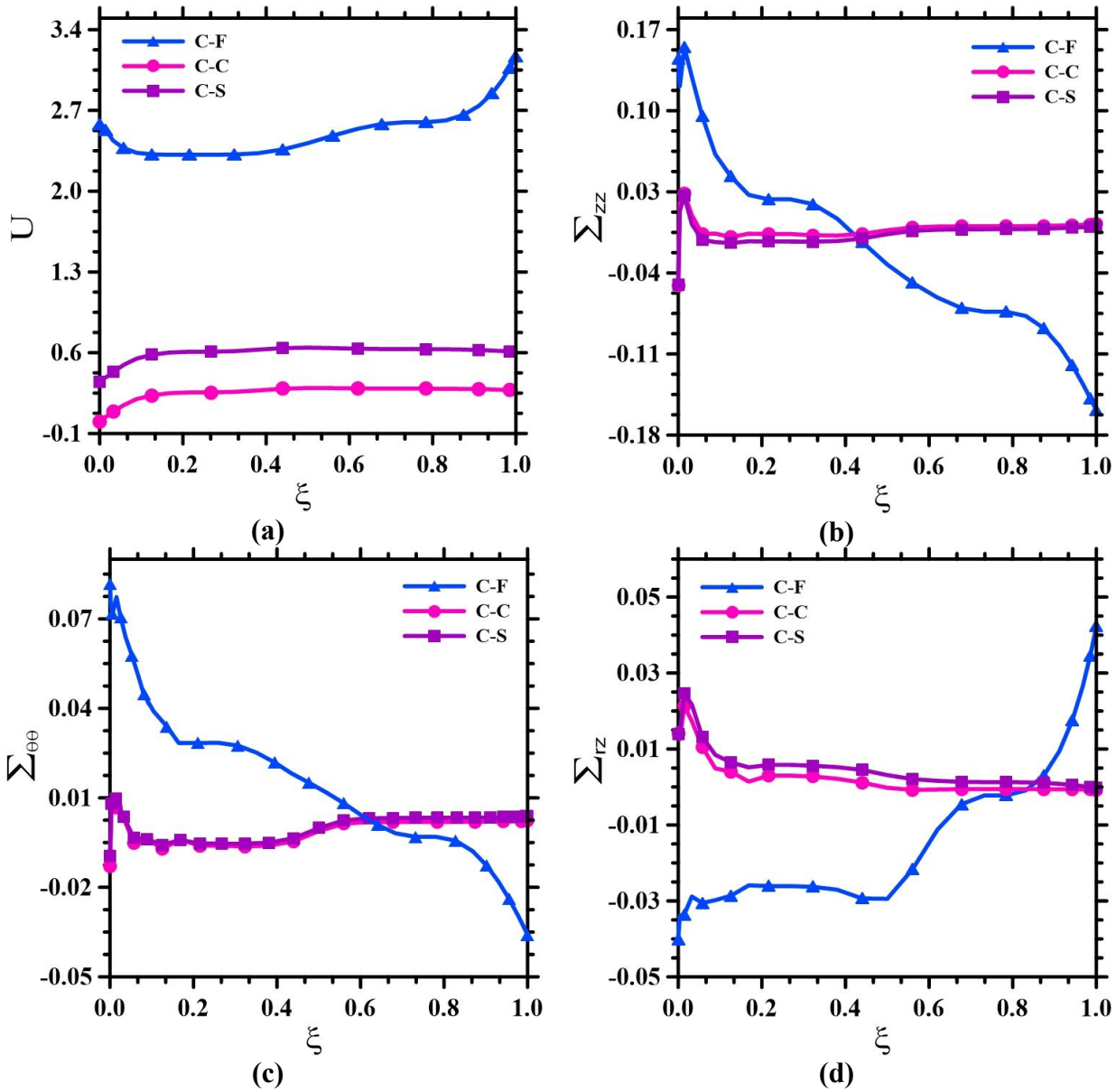

Fig. 18: Effects of the boundary conditions on the through-the-thickness variation of the results of the multilayer truncated conical shell with the GPLRC-FS and GPLRC-PC $\left[W_{GPL}=0.3\%,\right.$ $\eta=0.5,\ Fo=1,\ e_0=0.4,$ porosity type 1, $\beta=15^{\circ},\ u^{*}=1(\text{cm/s}),\ \tau=0.03\left.\right]$.

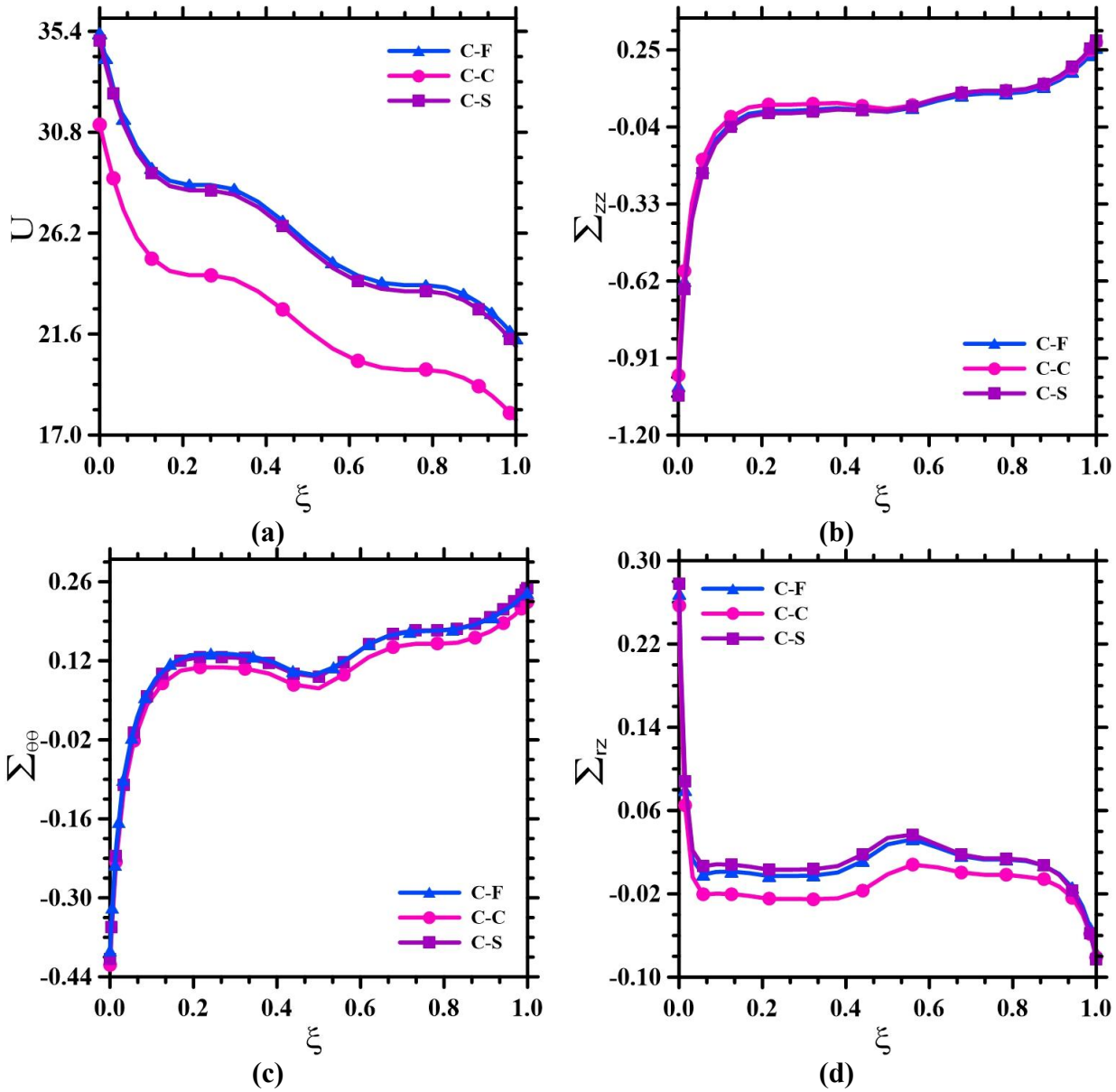

Fig. 19: Effects of the boundary conditions on the through-the-thickness variation of the results of the multilayer truncated conical shell with the GPLRC-FS and GPLRC-PC $\left[W_{GPL}=0.3\%,\right.$ $\eta=0.5,\ Fo=0.5,\ e_0=0.4,$ porosity type 1, $\beta=15^{\circ},\ u^{*}=1(\text{cm/s}),\ \tau=0.03\left.\right]$.

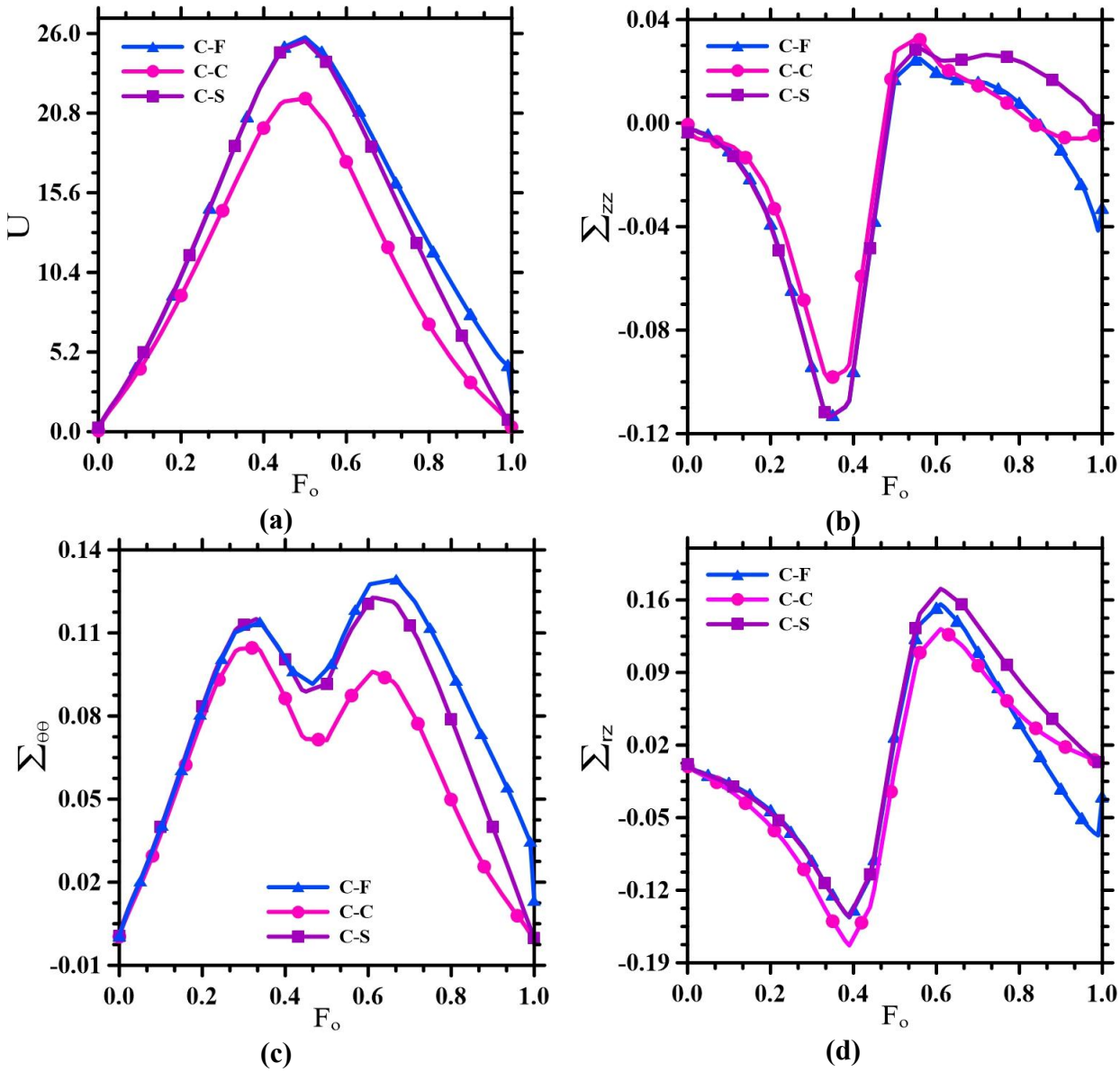

Fig. 20: Effects of the boundary conditions on the time histories of the results of the multilayer truncated conical shell with the GPLRC-FS and GPLRC-PC $\left[W_{GPL}=0.3\%,\ \zeta=0.5,\eta=0.5,\right.$ $\left.e_0=0.4,\ \text{porosity type 1},\beta=15^{\circ},\ u^*=1(\text{cm/s}),\ \tau=0.03\right]$.